



# Flare Duty Cycle of Gamma-Ray Blazars and Implications for High-energy Neutrino Emission

Kenji Yoshida<sup>1</sup> , Maria Petropoulou<sup>2,3</sup> , Kohta Murase<sup>4,5,6</sup> , and Foteini Oikonomou<sup>7</sup> <sup>1</sup> Department of Electronic Information Systems, Shibaura Institute of Technology, 307 Fukasaku, Minuma-ku, Saitama, Japan; [yoshida@shibaura-it.ac.jp](mailto:yoshida@shibaura-it.ac.jp)<sup>2</sup> National and Kapodistrian University of Athens, 157 72, Athens, Greece<sup>3</sup> Institute of Accelerating Systems & Applications, University Campus Zografos, Athens, Greece<sup>4</sup> Department of Physics; Department of Astronomy & Astrophysics; Center for Multimessenger Astrophysics, Institute for Gravitation and the Cosmos, The Pennsylvania State University, University Park, PA, USA<sup>5</sup> School of Natural Sciences, Institute for Advanced Study, Princeton, NJ, USA<sup>6</sup> Center for Gravitational Physics and Quantum Information. Yukawa Institute for Theoretical Physics, Kyoto, Japan<sup>7</sup> Physics Department, Norwegian University of Science and Technology, NO-7491, Trondheim, Norway

Received 2022 October 18; revised 2023 June 14; accepted 2023 July 5; published 2023 September 6

## Abstract

Gamma-ray flares of blazars may be accompanied by high-energy neutrinos due to interactions of high-energy cosmic rays in the jet with photons, as suggested by the detection of the high-energy neutrino IceCube-170922A during a major gamma-ray flare from blazar TXS 0506+056 at the  $\sim 3\sigma$  significance level. In this work, we present a statistical study of gamma-ray emission from blazars to constrain the contribution of gamma-ray flares to their neutrino output. We construct weekly binned light curves for 145 gamma-ray bright blazars in the Fermi Large Area Telescope Monitored Source List adding TXS 0506+056. We derive the fraction of time spent in the flaring state (flare duty cycle) and the fraction of energy released during each flare from the light curves with a Bayesian blocks algorithm. We find that blazars with lower flare duty cycles and energy fractions are more numerous among our sample. We identify a significant difference in flare duty cycles between blazar subclasses at a significance level of 5%. Then using a general scaling relation for the neutrino and gamma-ray luminosities,  $L_\nu \propto (L_\gamma)^\gamma$  with a weighting exponent of  $\gamma = 1.0\text{--}2.0$ , normalized to the quiescent gamma-ray or X-ray flux of each blazar, we evaluate the neutrino energy flux of each gamma-ray flare. The gamma-ray flare distribution indicates that blazar neutrino emission may be dominated by flares for  $\gamma \gtrsim 1.5$ . The neutrino energy fluxes for 1 week and 10 yr bins are compared with the decl.-dependent IceCube sensitivity to constrain the standard neutrino emission models for gamma-ray flares. Finally, we present the upper-limit contribution of blazar gamma-ray flares to the isotropic diffuse neutrino flux.

*Unified Astronomy Thesaurus concepts:* [Blazars \(164\)](#); [Gamma-ray astronomy \(628\)](#); [High energy astrophysics \(739\)](#); [Neutrino astronomy \(1100\)](#)

*Supporting material:* machine-readable table

## 1. Introduction

In 2013, the IceCube Neutrino Observatory discovered an all-sky flux of astrophysical neutrinos with energies from  $\sim 100$  TeV to several PeV (Aartsen et al. 2013a, 2013b). Since then, the spectrum of this high-energy neutrino flux has been measured to a higher precision with different analyses (e.g., Aartsen et al. 2015a, 2016, 2020a). The nearly isotropic distribution of the neutrino arrival directions constrains a Galactic contribution to the measured IceCube flux to the level of  $\sim 10\%$  (Albert et al. 2018) supporting an extragalactic origin (e.g., Aartsen et al. 2014, 2015b).

Many proposals have been put forward to explain the diffuse neutrino flux as the cumulative emission from a population of sources, with several of them even predating its discovery (for recent reviews, see Ahlers & Halzen 2017; Mészáros 2017). Blazars, namely active galactic nuclei (AGNs) with relativistic jets closely aligned to our line of sight (Urry & Padovani 1995), belong to this long list of candidate sources. Due to their powerful magnetized jets and copious radiation fields, blazars are promising sites for high-energy neutrino production (see

reviews, e.g., Murase 2017; Murase & Stecker 2022, and references therein).

In 2017, IceCube detected a muon neutrino event with most probable energy of  $\sim 290$  TeV, IceCube-170922A, in spatial and temporal coincidence with a flaring gamma-ray blazar, TXS 0506+056, at the statistical significance level of  $3\sigma$  (IceCube Collaboration et al. 2018a). Prior to the 2017 flaring event, the IceCube Collaboration also reported  $3.5\sigma$  evidence for a neutrino excess on top of the atmospheric background expectation from the direction of TXS 0506+056 with an archival search of past IceCube data (IceCube Collaboration et al. 2018b). In addition, some blazars may be powerful enough to produce a strong point-source neutrino signal during flares and have been associated with high-energy neutrinos (Dermer et al. 2014; Kadler et al. 2016; Petropoulou et al. 2016; Gao et al. 2017; Oikonomou et al. 2019; Paliya et al. 2020; Petropoulou et al. 2020; Oikonomou et al. 2021; Rodrigues et al. 2021; Sahakyan et al. 2022).

Clustering limits (Murase & Waxman 2016; Capel et al. 2020) and stacking limits (Aartsen et al. 2017a; Neronov et al. 2017; Hooper et al. 2019; Smith et al. 2021; Abbasi et al. 2022) suggest that blazars are unlikely to be the dominant sources of the diffuse astrophysical neutrino flux detected by IceCube (Murase et al. 2018; Palladino et al. 2019; Yuan et al. 2020). However, they may still appear in stacking analyses of



Original content from this work may be used under the terms of the [Creative Commons Attribution 4.0 licence](#). Any further distribution of this work must maintain attribution to the author(s) and the title of the work, journal citation and DOI.

radio-bright blazar arrival directions (Hovatta et al. 2021; Plavin et al. 2021; Zhou & Kamionkowski 2021; Buson et al. 2022), which may support that the dominant neutrino sources are gamma-ray hidden or opaque (Murase et al. 2016), or the correlation level may be explained by a handful of the brightest blazars (Murase et al. 2014). The role of blazar flaring activity in neutrino-source associations is not yet fully understood. Moreover, the results of most stacking analyses are relevant to the time-average blazar emission. Murase et al. (2018) estimated the contribution of blazar flares like the 2017 multimessenger flare of TXS 0506+056 to the diffuse neutrino flux to be up to  $\sim 10\%$  based on the Fermi All-sky Variability Analysis (FAVA), but the constraint on the contribution from all blazar flares is very uncertain because it is affected by different assumptions (Yuan et al. 2020).

In this paper, we expand upon the work of Murase et al. (2018) by computing the duty cycle and the energy output fraction of gamma-ray flares using a much larger sample of blazars observed by the Large Area Telescope (LAT) on board the Fermi satellite. To estimate the neutrino flux during gamma-ray flares, we use a generic relationship between the all-flavor neutrino and gamma-ray fluxes, i.e.,  $F_\nu^{\text{fl}} \propto (F_\gamma^{\text{fl}})^\gamma$ , where  $1 \leq \gamma \leq 2$  (see also Yuan et al. 2020). We explore two cases depending on the definition of the neutrino flux in nonflaring periods (i.e., quiescence). First, we study the case where the neutrino flux outside flares is benchmarked with the quiescent gamma-ray flux, which has been widely adopted prior to the TXS 0506+056 observations (e.g., Murase et al. 2014; Padovani et al. 2015; Petropoulou et al. 2015). Second, motivated by the modeling studies of TXS 0506+056, we consider a case where the nonflaring neutrino flux is bound by the quiescent X-ray flux. Besides the usual  $E_\nu^{-2}$  power-law neutrino spectrum, we consider for both scenarios the effects of realistic neutrino spectra, using a spectral template derived for the multimessenger flare of TXS 0506+056. By comparing our neutrino predictions for each blazar in the sample to the time-integrated 10 yr IceCube sensitivity and the IceCube sensitivity for transient searches (scaled to 1 week), we constrain the aforementioned scenarios. We finally compute the contribution of blazar flares to the all-sky diffuse neutrino flux.

This paper is structured as follows. In Section 2, we describe the sample and the Fermi-LAT analysis for generating the light curves. We describe next how we define gamma-ray flaring states using the binned LAT light curves and present our results about the duty cycle of flares and their energy output fraction in Section 3. We discuss the implications of our results on the high-energy neutrino emission from flaring blazars in Section 4. We conclude in Section 5 with a summary of our results. In this work, we adopt a flat  $\Lambda$ CDM cosmology with  $H_0 = 70 \text{ km s}^{-1} \text{ Mpc}^{-1}$ , and  $\Omega_m = 0.30$ .

## 2. Gamma-Ray Data and Analysis

### 2.1. Data Selection

We select 145 gamma-ray bright blazars (Table A1), consisting of 106 flat spectrum radio quasars (FSRQs), 31 BL Lac objects, and 8 blazar candidates of uncertain type (BCUs). Among them, the 144 blazars are selected from the Fermi LAT Monitored Source List,<sup>8</sup> which we identified as blazars with the Fourth Catalog of AGN detected by the LAT (4LAC-DR2, hereafter 4LAC; Ajello et al. 2020). The Fermi-

LAT team monitors the light curves of a number of bright and transient sources that have flares during the mission to facilitate follow-up multiwavelength observations of flaring sources. When sources exceed the monitoring flux threshold of  $1 \times 10^{-6} \text{ cm}^{-2} \text{ s}^{-1}$ , they are added to the list of monitored sources.<sup>9</sup> Since blazars are known for their intense flares, the list gives the appropriate blazar samples that have flaring fluxes with high statistics. In addition, we added one blazar of TXS 0506+056, whose flaring state is indicated to be in coincidence with IceCube-170922A (IceCube Collaboration et al. 2018a). Our sample comprises the brightest blazars in the 4LAC catalog as shown in Figure 1. In this figure, we show the time-average energy flux in the energy range of 0.1–100 GeV based on 10 yr of data as a function of redshift for our sample and all blazars in the 4LAC. In this work, we analyze data collected by the LAT for the period 2009–2018 as described in the next section.

### 2.2. Fermi LAT Analysis

The Fermi LAT is a pair conversion telescope sensitive to gamma rays in the 20 MeV to  $>300$  GeV energy range (Atwood et al. 2009). In this work, we analyze the LAT data from MJD 54682 to MJD 58739 using the Fermi Science Tools version 11-05-03<sup>10</sup> and Fermipy version 0.17.3 (Wood et al. 2017). Following the standard selection recommendation,<sup>11</sup> we select photons with energies between 100 MeV and 316 GeV that were detected within a radius of  $20^\circ$  centered on the position of the source of interest, while photons detected with a zenith angle larger than  $90^\circ$  with respect to the spacecraft were discarded to reduce the Earth-limb gamma-ray contamination.

The contribution from isotropic and Galactic diffuse backgrounds is modeled using the parameterization provided in the `iso_P8R3_SOURCE_V2_v01.txt` and `gll_iem_v07.fits` files, respectively, leaving their all parameters free to vary in the spectral fit. Sources in the 4FGL catalog within a radius of  $15^\circ$  from the source position are included in the model with their spectral parameters fixed to their catalog values (Abdollahi et al. 2020), while the normalization of sources within  $3^\circ$  is allowed to vary freely during the spectral fit. The spectral fit is performed with a binned likelihood method using the `P8R3_SOURCE_V2` instrument response function with parameterization from 4FGL to characterize the spectral parameters of the source of interest in the 100 MeV–316 GeV energy range.

The gamma-ray light curve for each source is built with an end-to-end analysis in each time bin using the same processing steps as the spectral analysis. The period between MJD 54682 and MJD 58739 is divided into  $\sim 570$  7 days-long bins. A model spectral fit<sup>12</sup> is performed in each time bin with the free model parameters. The best-fit parameters are then used to calculate the gamma-ray flux in the 0.1–316 GeV energy range for each time bin of the light curve.

Figure 2 shows examples of gamma-ray light curves for four blazars, including the first plausible cosmic neutrino source,

<sup>9</sup> [https://fermi.gsfc.nasa.gov/ssc/data/access/lat/msl\\_lc/](https://fermi.gsfc.nasa.gov/ssc/data/access/lat/msl_lc/)

<sup>10</sup> <http://fermi.gsfc.nasa.gov/ssc/data/analysis/software>

<sup>11</sup> [https://fermi.gsfc.nasa.gov/ssc/data/analysis/documentation/Cicerone/Cicerone\\_Data\\_Exploration/Data\\_preparation.html](https://fermi.gsfc.nasa.gov/ssc/data/analysis/documentation/Cicerone/Cicerone_Data_Exploration/Data_preparation.html)

<sup>12</sup> The spectral models used are from the 4FGL, e.g., PowerLaw, LogParabola, and PLSuperExpCutoff. In LogParabola, the free parameters are norms,  $\alpha$ , and  $\beta$ .

<sup>8</sup> [https://fermi.gsfc.nasa.gov/ssc/data/access/lat/msl\\_lc/](https://fermi.gsfc.nasa.gov/ssc/data/access/lat/msl_lc/)

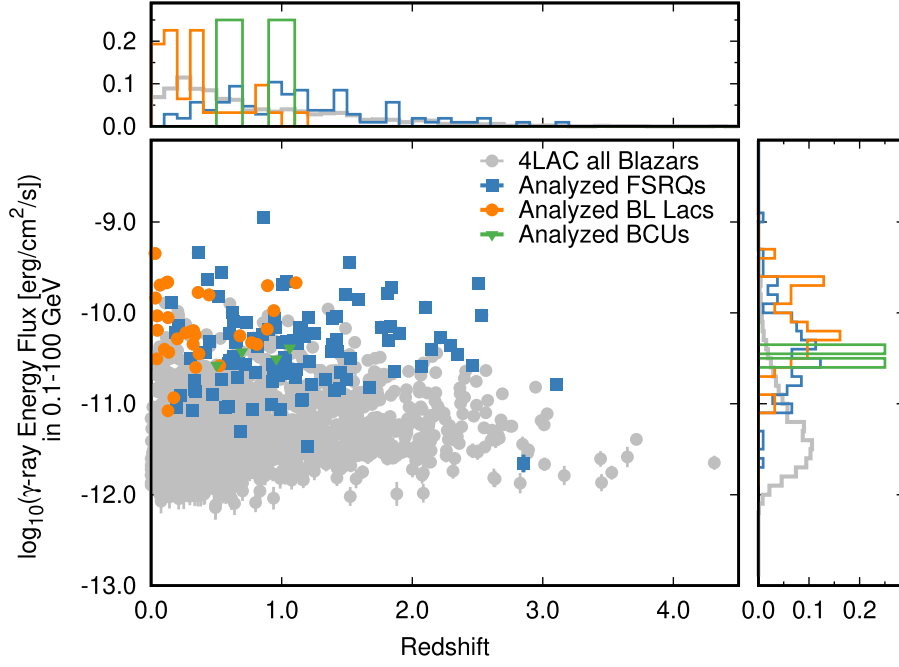


**Figure 1.** Scatter diagram of the time-average gamma-ray energy flux and redshift for the 145 blazars in our sample (106 FSRQs in blue, 31 BL Lac objects in orange, and 8 BCUs in green). All blazars in the 4LAC are overlaid (gray markers) for comparison reasons. Side panels show the projected histograms on each axis. The energy fluxes are taken from 4LAC, and the redshifts are from 4LAC and SIMBAD (Oberto et al. 2019).

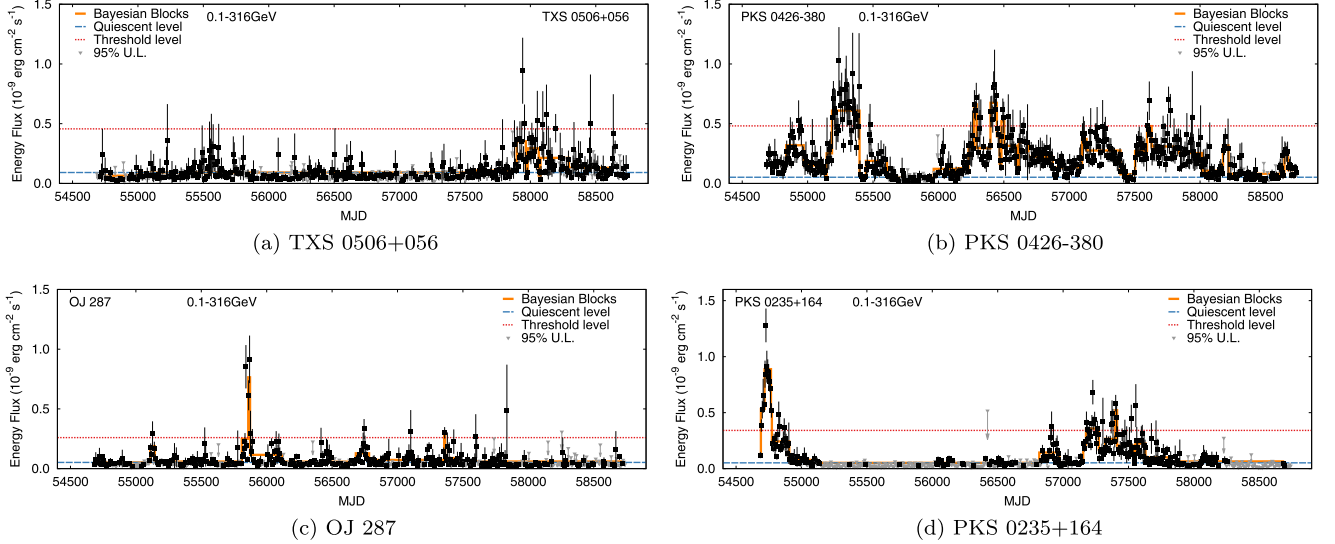


**Figure 2.** Indicative examples of weekly binned blazar gamma-ray light curves (black points) in the 0.1–316 GeV energy range. Gray triangles indicate 95% upper limits. The quiescent flux and flare threshold levels are plotted with dashed blue and red lines, respectively (for a definition of both flux thresholds, see Section 3.1). The Bayesian blocks’ representation of each light curve is overlotted with orange solid lines. The 1–316 GeV light curves of the same sources can be found in Appendix B.

TXS 0506+056. In all light curves, we show flux points with their  $1\sigma$  uncertainties (black symbols), if the source is detected with a test statistic larger than 9 (corresponding to a  $3\sigma$  excess) and the flux in one bin is larger than its uncertainty. Otherwise, we show the flux upper limits at the 95% confidence level.

### 3. Gamma-Ray Flare Distributions

In this section, we start by defining gamma-ray flaring states using the weekly binned Fermi LAT light curves (Section 3.1). We then derive the flare duty cycle (i.e., fraction of time spent in flaring states) and the flare energy fraction (i.e., fraction of energy released in flaring states) for all sources in our sample,

and discuss potential differences between BL Lac objects and FSRQs (Section 3.2). A comparison of our results with those reported by Murase et al. (2018) can be found in Appendix E.

#### 3.1. Definition of Flares

##### 3.1.1. Quiescent Flux Level

Although there is no rigorous way to define the quiescent flux level of blazar emission, it is reasonable to assume that the quiescent state has a relatively low and stable flux. In this study, we adopt the following procedure to derive the quiescent gamma-ray flux level of a blazar:

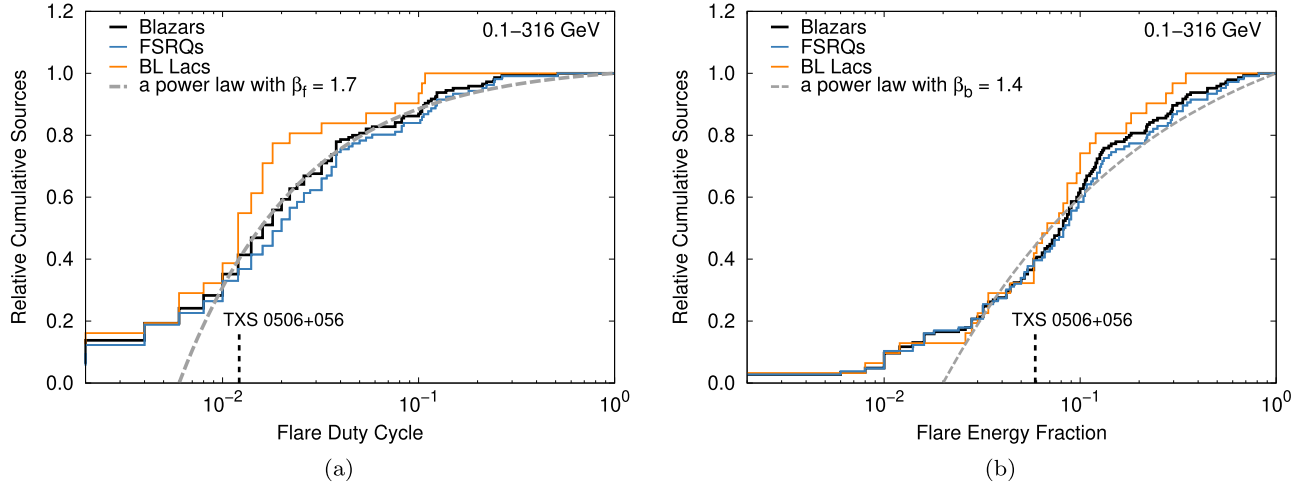


**Figure 3.** Cumulative histograms (normalized to one) of the 0.1–316 GeV gamma-ray flare duty cycles (a) and flare energy fractions (b) of 145 blazars (black solid histogram), 106 FSRQs (blue solid histogram), and 31 BL Lac objects (orange solid histogram). In both panels, the vertical dashed line indicates the values for TXS 0506+056. The dashed gray lines depict cumulative power-law functions (see text for more details).

1. We apply a Bayesian blocks algorithm to each gamma-ray light curve with a false alarm probability  $p_0 = 0.05$ , adopting the so-called point measurements fitness function for the Bayesian blocks algorithm (Astropy Collaboration et al. 2013; Scargle et al. 2013; Astropy Collaboration et al. 2018).
2. The Bayesian blocks algorithm provides the partitions of the light curve into blocks where the flux is regarded to be constant. This is an optimal step-function representation of the light curve.
3. We consider the minimum average flux as a representative of the source quiescent flux, under the following condition: the number of data points within the selected block is more than or equal to a half of the average number of data points of all other blocks. This condition prevents us from using an insufficient amount of data points to estimate the quiescent flux level. We note that the quiescent flux levels hardly depend on the choice of  $p_0$  (in the range 0.01–0.1) as described in Section 3.1.2.

Figure 2 shows indicative examples of weekly binned Fermi LAT light curves from our sample (black points) and the Bayesian blocks’ representations (solid orange lines). The quiescent flux levels derived using the method described above are also indicated with dashed cyan lines. To verify the quiescent flux level being identified properly, we derived the gamma-ray quiescent fluxes by using coarser time binning for the light curves. See Appendix C for details.

### 3.1.2. Flaring Threshold Level

Various definitions of flaring states in blazar emission exist in the literature (e.g., Resconi et al. 2009; Nalewajko 2013; Meyer et al. 2019; Stathopoulos et al. 2022). Here, we define, as a gamma-ray flare, any flux point of the weekly binned light curve that exceeds a certain threshold,  $F_\gamma^{\text{th}}$ , given by

$$F_\gamma^{\text{th}} = F_\gamma^q + s \langle F_\gamma^{\text{err}} \rangle, \quad (1)$$

where  $F_\gamma^q$  is the gamma-ray quiescent flux level,  $\langle F_\gamma^{\text{err}} \rangle$  is the average uncertainty of the gamma-ray fluxes,<sup>13</sup> and  $s$

corresponds to the significance above the quiescent flux level in units of the standard deviation  $\sigma$ . Unless otherwise noted, we use  $s = 6$  in this work. The flaring threshold levels are indicated with dotted red lines in Figure 2.

### 3.2. Flare Duty Cycle and Flare Energy Fraction

The fraction of time spent in the flaring state, i.e., the flare duty cycle, is defined as

$$f_{\text{fl}} = \frac{1}{T_{\text{tot}}} \int_{F_\gamma^{\text{th}}} dF_\gamma \frac{dT}{dF_\gamma}, \quad (2)$$

where  $T_{\text{tot}}$  is the total observation time,  $F_\gamma$  is the gamma-ray energy flux, and  $T$  is the time spent at the respective flux level. The fraction of energy emitted in the flaring state, i.e., the gamma-ray flare energy fraction, is given by Murase et al. (2018):

$$b_{\text{fl}}^\gamma = \frac{1}{F_\gamma^{\text{ave}} T_{\text{tot}}} \int_{F_\gamma^{\text{th}}} dF_\gamma F_\gamma \frac{dT}{dF_\gamma} \quad (3)$$

where  $F_\gamma^{\text{ave}}$  is the average gamma-ray energy flux over the whole observation period. Note that Murase et al. (2018) introduced the flare duty cycle and energy fraction with gamma-ray luminosity  $L_\gamma$ .

Figure 3 shows the cumulative distributions of the 0.1–316 GeV gamma-ray flare duty cycles ( $f_{\text{fl}}$ ) and flare energy fractions ( $b_{\text{fl}}^\gamma$ ) of 145 blazars (106 FSRQs, 31 BL Lac objects, and 8 BCUs). The  $f_{\text{fl}}$  and  $b_{\text{fl}}^\gamma$  values for TXS 0506+056 are indicated with vertical dashed lines. TXS 0506+056 belongs to the 30% (40%) of the cumulative distribution of the flare duty cycle (flare energy fraction). Thus, TXS 0506+056 is not an extraordinary source in terms of its gamma-ray flaring activity. We also perform a two-sample Kolmogorov–Smirnov (K-S) test to check if the cumulative distributions of either  $f_{\text{fl}}$  or  $b_{\text{fl}}^\gamma$  are the same for FSRQs and BL Lacs. Under the null hypothesis that the FSRQ and BL Lac distributions are derived from the same parent distribution, the probabilities are  $p = 0.039$  for the flare duty cycles distributions with the K-S statistic  $D = 0.279$ , and  $p = 0.521$  for the gamma-ray flare energy fraction distributions, with  $D = 0.159$ , respectively. Hence, we can reject the null hypothesis that the distributions of flare duty cycles for FSRQs

<sup>13</sup>  $\langle F_\gamma^{\text{err}} \rangle = (\sum_{i=1}^N \sigma_i) / N$ , where  $N$  is the number of time bins of a light curve, and  $\sigma_i$  is the flux uncertainty of the  $i$ th time bin.

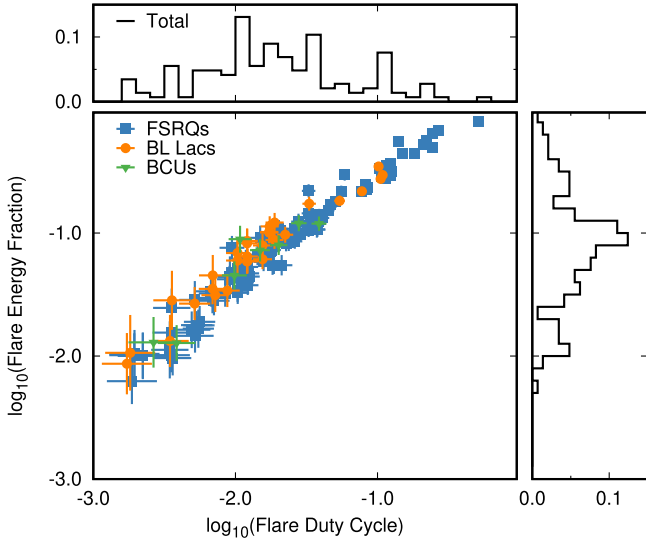


**Figure 4.** Scatter plot of the 0.1–316 GeV gamma-ray flare duty cycles and flare energy fractions of 141 blazars (103 FSRQs in blue squares, 30 BL Lac objects in orange circles, and 8 BCUs in green triangles). Side panels show the projected histograms on each axis.

and BL Lac objects are drawn from the same parent population at a significance level of 5%. On the other hand, we cannot exclude the null hypothesis for the flare energy fractions of FSRQs and BL Lac objects at a significance level of 10%.

Figure 4 shows a strong correlation between the flare duty cycles ( $f_{\text{fl}}$ ) and the flare energy fractions ( $b_{\text{fl}}^{\gamma}$ ) of 141 blazars (103 FSRQs, 30 BL Lac objects, and 8 BCUs); here, the nonflaring sources are excluded at the  $6\sigma$  threshold. We find an almost linear relation between the two quantities for  $f_{\text{fl}} \lesssim 0.1$ , which however becomes sublinear for higher flaring duty cycles. The side panels of Figure 4 show histograms of the logarithm of the flare duty cycle and energy fraction. It can be shown that both distributions are well represented by power-law functions, namely  $dN/df_{\text{fl}} \propto f_{\text{fl}}^{-\beta_f}$  for  $f_{\text{fl}} \gtrsim 0.01$  and  $dN/db_{\text{fl}}^{\gamma} \propto (b_{\text{fl}}^{\gamma})^{-\beta_b}$  for  $b_{\text{fl}}^{\gamma} \gtrsim 0.03$ , with  $\beta_f \sim 1.7$  and  $\beta_b \sim 1.4$ . In other words, the blazars with lower flare duty cycles and flare energy fractions are more common in the sample compared to sources that are commonly flaring in gamma rays. Figure 3 also depicts the cumulative power-law functions with  $\beta_f = 1.7$  for 0.006–1.0 flare duty cycles, and  $\beta_b = 1.4$  for 0.02–1.0 flare energy fractions.

So far, we have presented results for  $f_{\text{fl}}$  and  $b_{\text{fl}}^{\gamma}$  obtained using the  $6\sigma$  threshold for the definition of flares. To check how our results depend on the choice for  $s$ , we construct the cumulative histograms of both quantities for integer values of  $s$  ranging from 2 to 9. Our results are shown in Figure 5. By lowering the threshold for the flaring flux, both  $f_{\text{fl}}$  and  $b_{\text{fl}}^{\gamma}$  distributions shift to higher values as expected. The duty cycle distribution tends to saturate only for  $s \geq 8$ . Still, for  $s \geq 6$ , we find small differences in the cumulative distributions of the duty cycle for  $f_{\text{fl}} \gtrsim 0.05$ . This suggests that our default choice of  $s = 6$  is sufficient for describing the high-end of the duty cycle distribution. The impact on the flare energy fraction distribution is smaller, as indicated by the smaller spread of the curves. For completeness, we also show the cumulative histograms for  $s = 6$  and two choices of the false alarm probability ( $p_0 = 0.01$  and 0.10) of the Bayesian block algorithm that we applied to the Fermi-LAT light curves (see

Section 3.1.1). The distributions are not sensitive to the choice of  $p_0$  at least for the values we consider.

Having determined the flare duty cycle for different blazar subclasses and having discussed the effects of the flare threshold value, we can now check if there is a correlation between the flare duty cycle and gamma-ray luminosity. In other words, we would like to check if the (quiescent) gamma-ray luminosity is a good indicator of the flaring activity of a blazar. We compute the quiescent gamma-ray luminosity as  $L_{\gamma}^q = 4\pi d_L^2 F_{\gamma}^q$  without the correction for extragalactic background light absorption, where  $d_L$  is the luminosity distance calculated with the redshift  $z$ , and  $F_{\gamma}^q$  is the 0.1–316 GeV gamma-ray quiescent flux (see Section 3.1.1). According to the 4FGL catalog, the blazars for  $z > 1.0$  show spectral turnovers less than 100 GeV, indicating that the extragalactic background light absorption is irrelevant. As an uncertainty in the flare duty cycle, we use the square root of the sum of squares of the flaring time-bin errors, which are half of the time-bin width, over the total observation time. As shown in Figure 6, there is no correlation between the gamma-ray flare duty cycle and the quiescent gamma-ray luminosity for neither blazar subclass. Similar results are found for different flare threshold values  $s = 2-9$ .

#### 4. Implications for High-energy Neutrino Emission

In order to discuss implications for neutrino emission, we need to know the physical relationship between neutrinos and gamma rays. In  $pp$  scenarios for either gamma-ray or neutrino data, neutrinos and gamma rays can be simply connected via the hadronic production process itself (Murase et al. 2013). However, blazar gamma-ray emission is usually explained by primary leptonic emission (e.g., inverse Compton scattering) and/or secondary cascade emission from photohadronic ( $p\gamma$ ) interactions, thus making the multimessenger connection much more model dependent. It is therefore useful to parameterize the multimessenger relationship in a generic manner using the luminosity weighting factor  $\gamma$  (e.g., Yuan et al. 2020)

$$L_{\nu}^{\text{fl}} = L_{\nu}^q \left( \frac{L_{\gamma}^{\text{fl}}}{L_{\gamma}^q} \right)^{\gamma}, \quad (4)$$

where  $L_{\nu}^{\text{fl}}$  is the flare neutrino luminosity,  $L_{\nu}^q$  is the quiescent neutrino luminosity, and  $L_{\gamma}^{\text{fl}}$  is the gamma-ray luminosity in the flaring state. Theoretical models typically predict  $\gamma \sim 1.0-2.0$  (e.g., Murase et al. 2018). Note that the differential gamma-ray energy flux,  $F_{E_{\gamma}}$ , is related to the bolometric gamma-ray luminosity as

$$L_{\gamma} = 4\pi d_L^2 \int dE_{\gamma} F_{E_{\gamma}}. \quad (5)$$

There are different ways to estimate the nonflaring (quiescent) neutrino flux,  $E_{\nu} F_{E_{\nu}}^q$ . In what follows, we explore two cases where  $E_{\nu} F_{E_{\nu}}^q$  is benchmarked with the quiescent gamma-ray flux (scenario (1)) or quiescent X-ray flux (scenario (2)). For each scenario, we consider the impacts of the neutrino spectrum. For illustration purposes, we present in Figure 7 a scatter plot of the quiescent gamma-ray and X-ray fluxes for 138 blazars of 101 FSRQs, 31 BL Lac objects, and 6 BCUs. Note that the majority of sources has  $E_{\gamma} F_{E_{\gamma}}^q > E_X F_{E_X}^q$ , which relates also to their broadband spectral types.

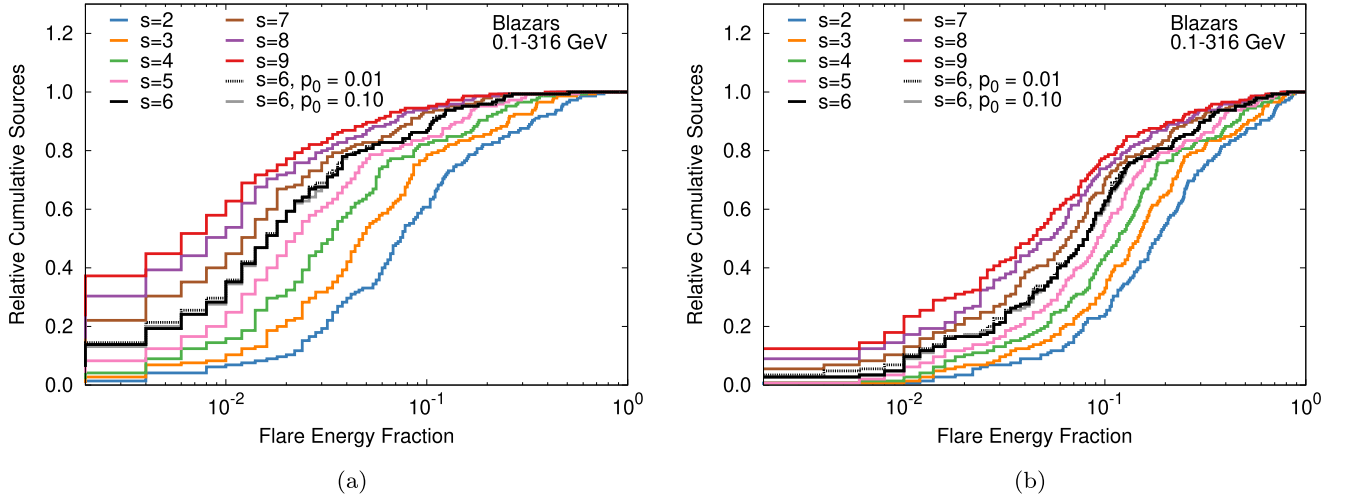


**Figure 5.** Cumulative histograms of the 0.1–316 GeV gamma-ray flare duty cycles (a) and flare energy fractions (b) of 145 blazars for different integer values of  $s$  ranging from 2 to 9. In the case of  $s = 6$ ; cumulative histograms of  $p_0 = 0.01, 0.10$  are also plotted.

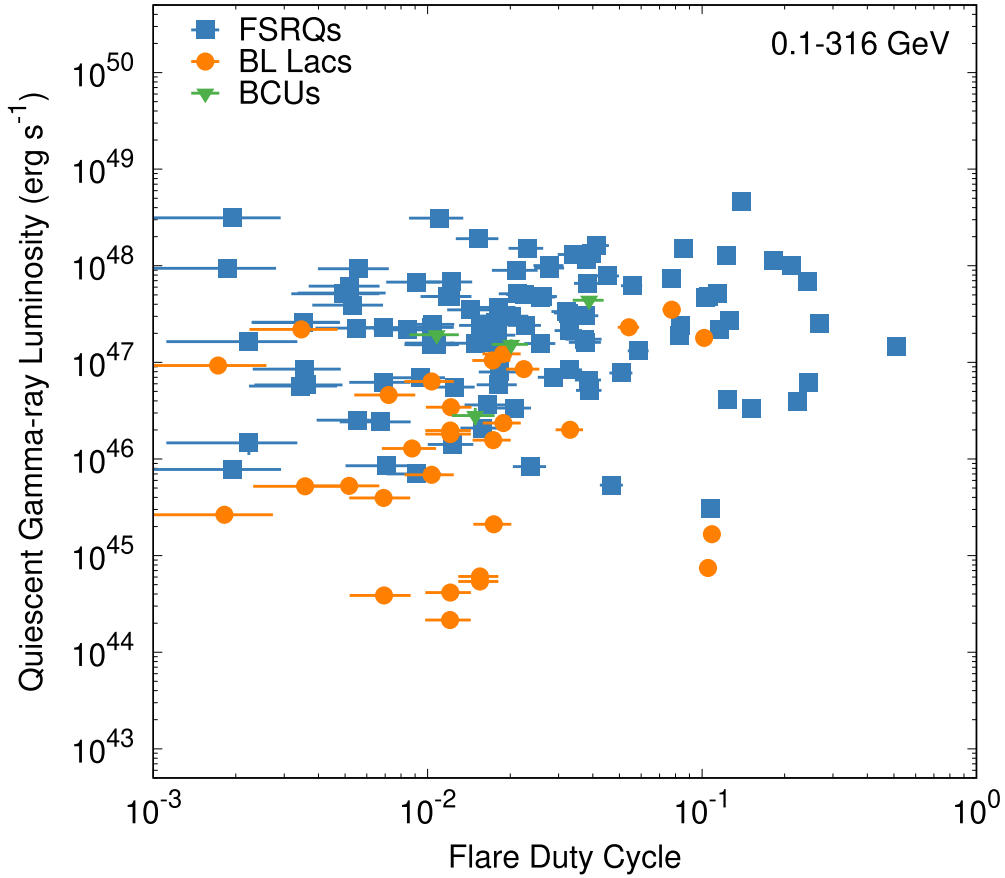


**Figure 6.** Scatter plot between 0.1–316 GeV gamma-ray flare duty cycle and quiescent gamma-ray luminosity for 137 blazars of 103 FSRQs (blue squares), 30 BL Lac objects (orange circles), and 4 BCUs (green triangles).

#### 4.1. Gamma-Ray Proxy (Scenario 1)

One of the ways to scale the neutrino luminosity is through the gamma-ray luminosity. Such a scaling is reasonable in hadronic models for gamma-ray emission, but it is nontrivial in leptonic models. Nevertheless, it may approximately hold given that the Compton dominance parameter is similar. The quiescent muon neutrino flux is benchmarked with the quiescent gamma-ray flux, and the flaring muon neutrino flux

is written as

$$E_{\nu_\mu} F_{E_{\nu_\mu}}^{\text{fl}} = E_{\nu_\mu} F_{E_{\nu_\mu}}^q \left( \frac{F_\gamma^{\text{fl}}}{F_\gamma^q} \right)^\gamma = A_\gamma \frac{E_\gamma F_{E_\gamma}^q}{3} \left( \frac{F_\gamma^{\text{fl}}}{F_\gamma^q} \right)^\gamma, \quad (6)$$

where  $A_\gamma$  is a normalization parameter, and the factor of 3 comes from neutrino flavor mixing in vacuum  $\nu_e : \nu_\mu : \nu_\tau \simeq 1 : 1 : 1$ . Here, we relate the differential quiescent neutrino flux at

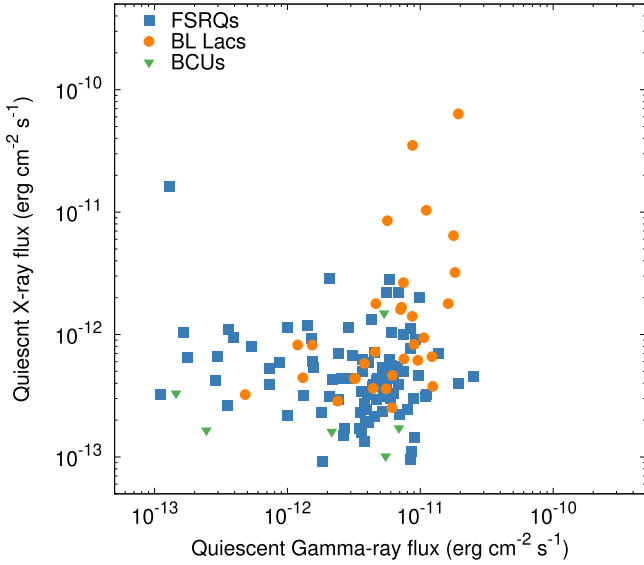


**Figure 7.** Scatter plot between the quiescent gamma-ray and X-ray fluxes for 138 blazars of 101 FSRQs (blue squares), 31 BL Lac objects (orange circles), and 6 BCUs (green triangles). The isolated upper left FSRQ is 3C 273.

300 TeV to the quiescent gamma-ray flux at the pivot energies for each weekly time bin. The pivot energies, which are chosen close to the decorrelation energy to minimize the correlation between the fitted gamma-ray spectral parameters, range from 0.1 to 316 GeV even in one source. The typical values are, however, 0.2–0.3 GeV. Then, the quiescent gamma-ray flux  $E_\gamma F_{E_\gamma}^q$  is estimated from the  $E_\gamma F_{E_\gamma}$  light curve at the pivot energies in the same way as the quiescent gamma-ray flux—see Section 3.1.1.

In photomeson production interactions in the blazar jet, the neutrinos and other secondaries produced via the neutral and charged pion decay chains carry comparable energy fluxes (see, e.g., Equations (13) and (14) of Murase et al. 2018). As a result, the neutrino energy flux is accompanied by a comparable energy flux of electromagnetic cascade emission at lower energies. However, not all X-rays and gamma rays are produced in photomeson production interactions. They may as well originate from Bethe–Heitler pair production and leptonic processes that are not accompanied by neutrinos. Therefore, we adopt  $A_\gamma = 1$  as an upper limit for the normalization parameter. A stronger upper limit on  $A_\gamma$  can be obtained from the nondetection of neutrinos from some of the blazars in our sample as illustrated in the following figures.

Figure 8 shows the estimated muon neutrino flare fluxes from scenario (1) with  $A_\gamma = 1.0$ , and  $\gamma = 1.5$  as a function of  $\sin(\delta)$ , where  $\delta$  is the source decl., neglecting the muon neutrino flux equal to or less than its uncertainty. The results for 1 week and 10 yr bins are shown in the left and right panels, respectively.<sup>14</sup> The neutrino flare fluxes for a 10 yr bin are the averages of the weekly neutrino flare fluxes, with zero fluxes assumed for the nonflaring states. For both binning choices, there are several blazar flares with predicted neutrino fluxes that exceed the IceCube sensitivity. The lack of neutrino detections from these sources can therefore be used to derive limits on the normalization  $A_\gamma$  for different values of the index  $\gamma$  (gray lines),

as demonstrated in Figure 9. As expected, the weaker the relation between neutrino and gamma-ray energy fluxes is (i.e., lower  $\gamma$  values), the higher  $A_\gamma$  can be. The red, orange, brown, and purple lines indicate stringent limits obtained for a couple of sources in our sample, such as 3C 454.3, 3C 279, PKS 1502 +106, and PKS 1510-089. The estimated neutrino flare fluxes with a 10 yr bin are lower than those with a 1 week bin because of the averaging. Meanwhile, the IceCube 90% sensitivity for a 10 yr bin is much lower than that for 1 week bin. Hence, the limits placed on  $A_\gamma$  from the 10 yr binning analysis are more stringent than those set by the weekly binned analysis.

#### 4.2. X-Ray Proxy (Scenario 2)

This case is motivated by modeling studies of the TXS 0506 +056 multimessenger observations of TXS 0506+056 (e.g., Keivani et al. 2018; Petropoulou et al. 2020), which demonstrated that the neutrino fluxes are bound by the X-ray data. The quiescent muon neutrino flux is benchmarked with the quiescent X-ray flux,  $E_X F_{E_X}^q$ , and the muon neutrino flare flux is written as

$$E_{\nu_\mu} F_{\nu_\mu}^{\text{fl}} = E_{\nu_\mu} F_{E_{\nu_\mu}}^q \left( \frac{F_\gamma^{\text{fl}}}{F_\gamma^q} \right)^\gamma = A_X \frac{E_X F_{E_X}^q}{3} \left( \frac{F_\gamma^{\text{fl}}}{F_\gamma^q} \right)^\gamma \quad (7)$$

where  $A_X$  is a normalization parameter. For  $\gamma = 1.0$ –2.0, we can set an upper limit on  $A_X$  so that our predictions are consistent with the nondetection of neutrinos from flares of individual blazars.

For the X-ray data, we use the Open Universe for Blazars, which provides blazar X-ray light curves based on 14 yr of Swift-XRT data (Giommi et al. 2019). The 0.5, 1.0, 1.5, 3.0, and 4.5 keV quiescent fluxes are estimated in the same way as the gamma-ray quiescent level (see Section 3.1.1). The X-ray quiescent flux,  $E_X F_{E_X}^q$ , is then defined as the average of the quiescent fluxes in these five energies. Figure D1 in Appendix D shows examples of the 1.0 keV X-ray light curves with the respective Bayesian blocks’ representations and quiescent fluxes. By using Equation (7), we derive the neutrino flare fluxes of 129 blazars (97 FSRQs, 26 BL Lac objects, 6 BCUs), ignoring 16 sources without flaring states found at the  $6\sigma$  threshold or without well-defined X-ray quiescent state.

In Figure 10, we plot the estimated muon neutrino flare fluxes from scenario (2) with  $A_X = 1.0$ , and  $\gamma = 1.5$  as a function of  $\sin(\delta)$ , for two binning choices (panels (a) and (b)). The estimated neutrino flare fluxes in scenario (2) are generally lower by 1 or 2 orders of magnitude than those in scenario (1) (compare to Figure 8). This result is related to the different spectral energy distributions (SEDs) of blazars in our sample. The majority of them are FSRQs, which are typically low-synchrotron peaked sources, and their SED has a trough in the X-ray band covered by Swift-XRT. As a result, the X-ray fluxes used as a proxy to scale the neutrino luminosity are lower than the gamma-ray fluxes used in scenario (1) (see also Figure 7). This does not apply, however, to MeV blazars and extreme synchrotron peaked sources (Costamante 2020). Figure 11 shows the normalization parameter  $A_X$  in gray as a function of the indices  $\gamma$  based on the nondetection of neutrino events, compared to the IceCube 90% sensitivity for 1 week binning (left) and 10 yr binning (right). The red, blue, green, and orange lines show sources with the lowest normalization parameters (see inset legend).

<sup>14</sup> In Appendix F, we also present the estimated muon neutrino flare fluxes using the gamma-ray photon fluxes instead of the gamma-ray energy fluxes.

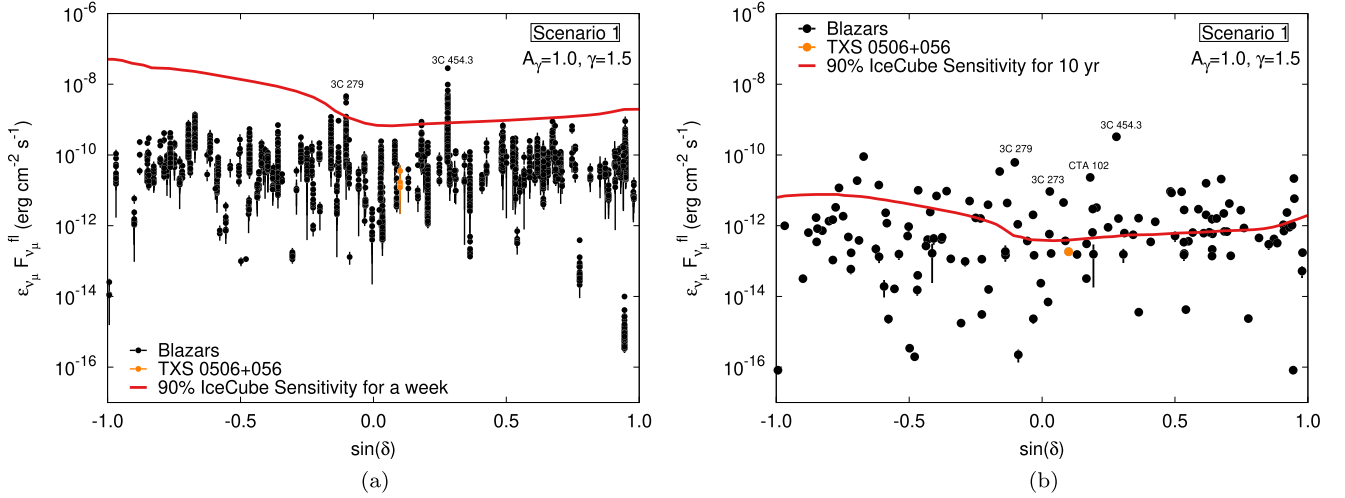


**Figure 8.** Estimated muon neutrino flare fluxes of 136 blazars (102 FSRQs, 26 BL Lac objects, and 8 BCUs) for a 1 week bin (a) and a 10 yr bin (b) of scenario (1) with  $A_\gamma = 1.0$ , and  $\gamma = 1.5$  as a function of  $\sin(\delta)$  where  $\delta$  is the source decl. The IceCube 90% sensitivities (red solid lines) for a point source with an  $E_\nu^{-2}$  neutrino spectrum for 1 week and 10 yr are taken from Vandenbroucke et al. (2019), Aartsen et al. (2020b), respectively.

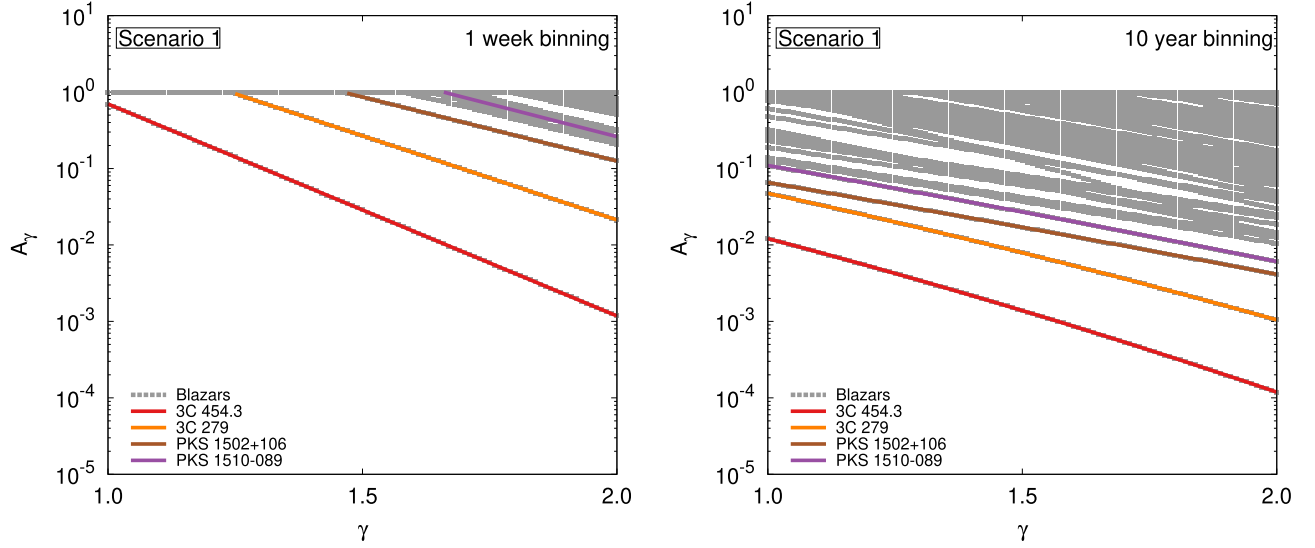


**Figure 9.** Upper limits on the normalization parameter  $A_\gamma$  of the analyzed blazars in gray as a function of the indices  $\gamma$  based on the nondetection of neutrino events, compared to the IceCube 90% sensitivity for scenario (1). The left and right panels show the normalization parameters with 1 week binning and 10 yr binning, respectively. When sources whose flares are all less than the sensitivity flux, the normalization parameters of  $A_\gamma$  are set to 1.0. The normalization parameter of the source is adjusted so that the maximum neutrino flux of the source is equal to the sensitivity flux if the flux of at least one flare exceeds the sensitivity. Several sources with the lowest normalization parameters are plotted with red, orange, brown, and purple lines.

### 4.3. Impacts of Realistic Spectra and Upper Limits

We also investigate the sensitivity of our results to a non-power-law shape of the neutrino spectrum. To this end, we assume a more realistic, albeit model-dependent neutrino spectrum motivated by lepto-hadronic models of TXS 0506+056. We compare the expected number of neutrinos to the one expected under the assumption of an  $E_\nu^{-2}$  neutrino spectrum, which we have used in the previous sections. We choose the LMBB2b model of Keivani et al. (2018) as an illustrative example of a characteristic neutrino spectrum that might result from photomeson production processes in the jet of a blazar during a gamma-ray flare.

We use Equations (6) and (7) with a 10 yr binning to test this variant of scenarios (1) and (2) respectively, and to place upper limits on the normalization parameters,  $A_\gamma$  and  $A_X$ . To calculate

the expected number of neutrinos, we assume the IC86 point-source effective area given in Aartsen et al. (2017b).

Columns (4)–(5) and (6)–(7) of Table 1 can also be used to see the effect of the more realistic spectral shape. For TXS 0506+056 and 3C 454.3, the expected number of neutrinos with the more realistic model is a factor of 2 lower than that of an  $E_\nu^{-2}$  neutrino spectrum. Therefore, the respective upper limits on  $A_\gamma$  and  $A_X$  of the more realistic model are a factor of 2 less stringent constraints. We thus conclude that the results obtained with our standard assumption of an  $E_\nu^{-2}$  spectral shape may be up to a factor of a few more strict for  $A_\gamma$  and  $A_X$  than with a different spectral shape for a given total neutrino energy flux. Regardless of the neutrino spectral template, the upper limits on  $A_{\gamma/X}^{\text{up}}$  are several orders of magnitude more constraining for 3C 454.3 than for TXS 0506+056.

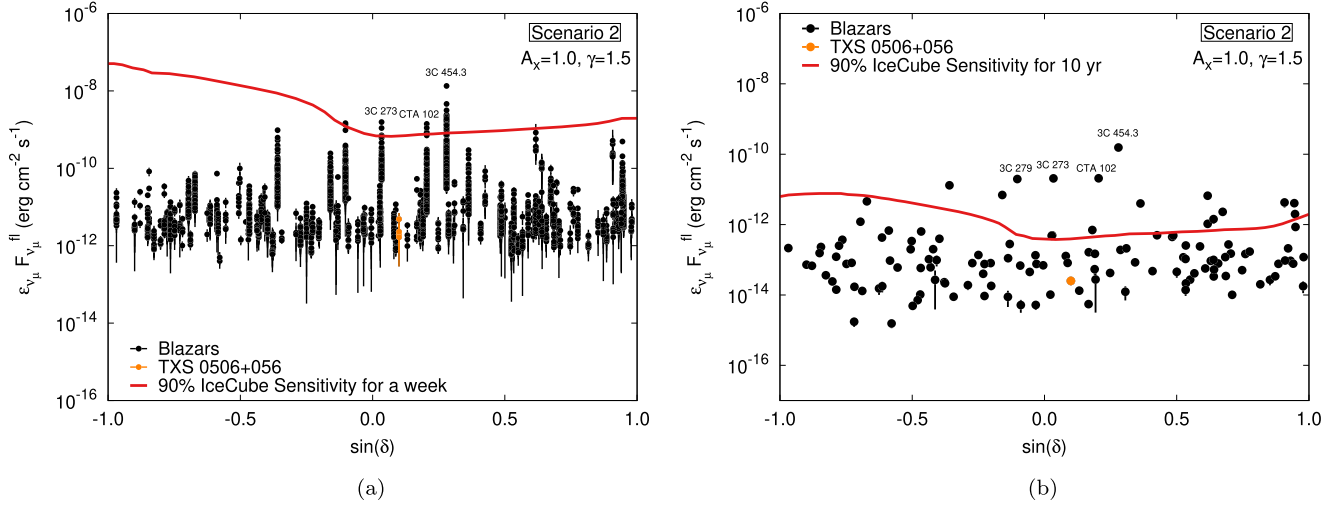


**Figure 10.** Estimated muon neutrino flare fluxes of 129 blazars (97 FSRQs, 26 BL Lac objects, and 6 BCUs) for a 1 week bin (a) and a 10 yr bin (b) of scenario (2) with  $A_X = 1.0$ , and  $\gamma = 1.5$  as a function of the  $\sin(\delta)$  with decl.  $\delta$ . The 90% IceCube sensitivities are the same as in Figure 8.

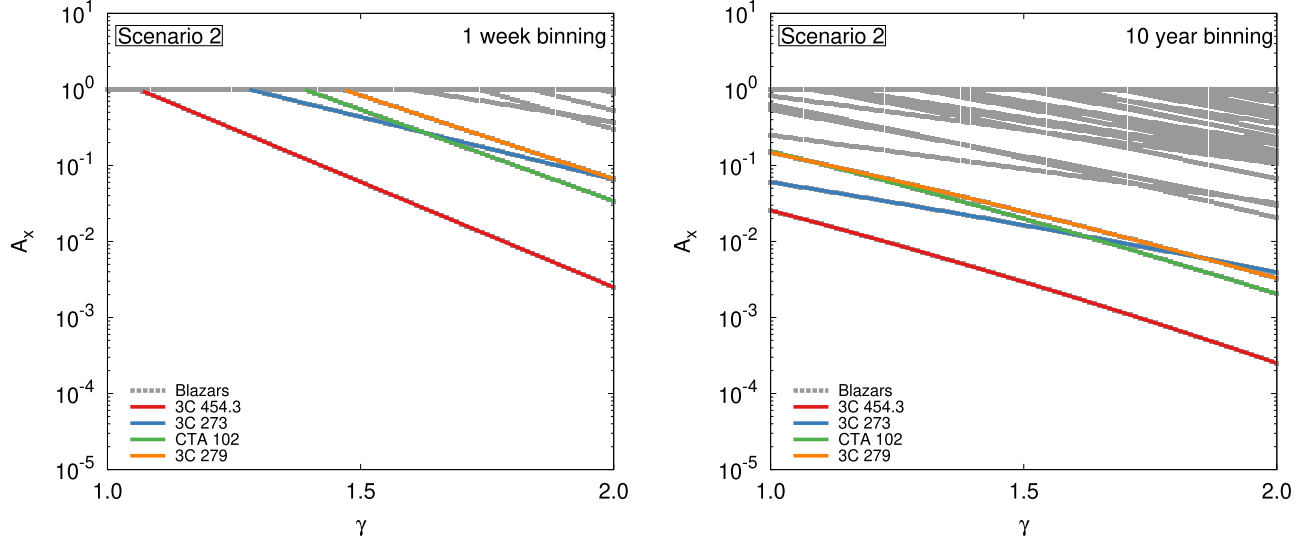


**Figure 11.** Upper limits on the normalization parameter  $A_X$  of the analyzed blazars in gray as a function of the indices  $\gamma$  based on the nondetection of neutrino events, compared to the IceCube 90% sensitivity for scenario (2). Left and right panels show the normalization parameters with 1 week binning and 10 yr binning, respectively. For sources whose flares are all less than the sensitivity flux, the normalization parameter  $A_X$  is set to 1.0. The normalization parameter of the source is adjusted so that the maximum neutrino flux of the source is equal to the sensitivity flux if the flux of at least one flare exceeds the sensitivity. Several sources with the lowest normalization parameters are plotted with red, blue, green, and orange lines.

**Table 1**  
Neutrino Counts Using the LMBB2b Model of Keivani et al. (2018; Columns 4, 5) and an  $E_\nu^{-2}$  Neutrino Spectrum (Columns 6, 7)

Source	Scenario	$\gamma$	LMBB2b		$E_\nu^{-2}$	
			$N_{\nu_\mu + \bar{\nu}_\mu} (A_{\gamma/X} = 1)$	$A_{\gamma/X}^{\text{up}} (90\% \text{ CL})$	$N_{\nu_\mu + \bar{\nu}_\mu} (A_{\gamma/X} = 1)$	$A_{\gamma/X}^{\text{up}} (90\% \text{ CL})$
TXS 0506+056	1	1.0	2	1	4	1
TXS 0506+056	1	1.5	6	1	10	1
TXS 0506+056	1	2.0	10	1	20	1
TXS 0506+056	2	1.0	0.3	1	0.5	1
TXS 0506+056	2	1.5	0.9	1	1.0	1
TXS 0506+056	2	2.0	2	1	3	1
3C 454.3	1	1.0	20	0.1	70	0.04
3C 454.3	1	1.5	200	$10^{-2}$	600	$4 \times 10^{-3}$
3C 454.3	1	2.0	2000	$10^{-3}$	6000	$4 \times 10^{-4}$
3C 454.3	2	1.0	10	0.2	30	0.08
3C 454.3	2	1.5	100	$2 \times 10^{-2}$	300	$8 \times 10^{-3}$
3C 454.3	2	2.0	1000	$2 \times 10^{-3}$	3000	$8 \times 10^{-4}$

**Note.** The assumed upper limit is 2.44 neutrinos in the livetime of IceCube. The IC86 point-source effective area has been assumed.

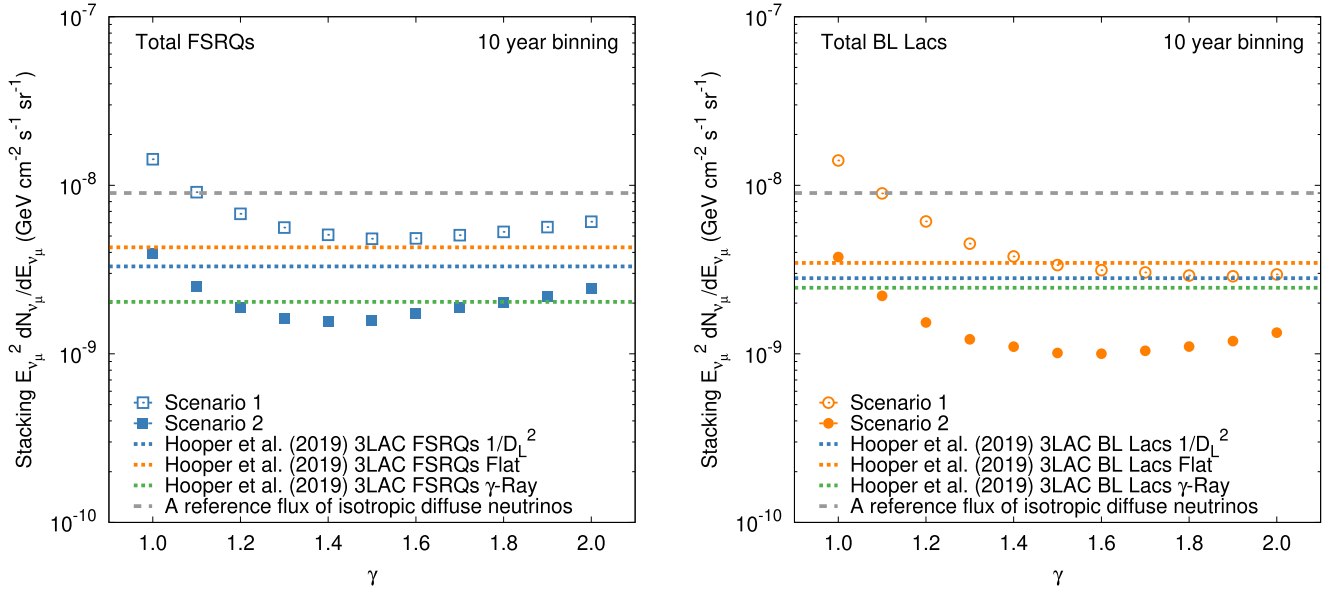


**Figure 12.** The total muon neutrino fluxes of gamma-ray flaring FSRQs and BL Lac objects as a function of  $\gamma$ . The total fluxes of muon neutrinos are estimated from our samples, multiplied by correction factors of the contribution of the 4LAC blazars and not-yet-detected blazars that are too gamma-ray faint to be included in the 4LAC catalog. The results of scenarios (1) and (2) are shown in open squares/circles and solid squares/circles, respectively, compared to a reference flux of all-sky muon neutrinos (gray dashed line; Aartsen et al. 2016). The three upper limits of Hooper et al. (2019) derived for different assumptions about the source evolution ( $1/D_L^2$ , Flat,  $\gamma$ -Ray), and reduced to 1/3 for muon neutrinos, are overplotted for comparison.

**Table 2**

Correction Factors for Determining the Contribution of Blazar Flares to the All-sky Neutrino Flux

$\gamma$	4LAC/Sample <sup>a</sup>		Total/4LAC <sup>b</sup>
	FSRQs	BL Lac Objects	
1.0	1.76	4.24	3.87
1.5	1.22	2.21	1.09
2.0	1.06	1.60	1.01

**Notes.**

<sup>a</sup> The correction factor of all the 4LAC FSRQs and BL Lac objects.

<sup>b</sup> The correction factor of the whole population of blazars.

#### 4.4. Contribution of Blazar Flares to the All-sky Neutrino Flux

There are two ways to examine the contribution of blazars to the all-sky neutrino flux. One is the stacking method considering the directions of IceCube neutrino events (Aartsen et al. 2017a; Hooper et al. 2019; Abbasi et al. 2022), and the other is the clustering analysis (Murase & Waxman 2016). Instead, our flux stacking method uses the estimated muon neutrino fluxes, not directly using the spatial correlation between the directions of IceCube neutrino events and blazars, but using the IceCube sensitivity at the decl. of each blazar in our sample.

As shown in Figures 8 and 10, some neutrino flare fluxes with  $A_\gamma = 1.0$ , and  $A_X = 1.0$  exceed the IceCube 90% sensitivity. The normalization parameters of  $A_\gamma$  and  $A_X$  are set to 1.0 for the sources whose flares are *all* less than the sensitivity flux. However, the normalization parameter of the source is reduced, if the flux of at least one flare exceeds the sensitivity, in a way that the maximum neutrino flux of the source is equal to the sensitivity flux.

In this work, we estimate the upper limits on the diffuse isotropic neutrino flux through flux stacking analyses of blazar flares. Our sample consists of bright gamma-ray blazars from

the 4LAC catalog as shown in Figure 1. There are fainter blazars in the 4LAC catalog, and there ought to be a lot of not-yet-detected blazars in the Universe.

To obtain the upper limits on the all-sky neutrino flux, the sum of the estimated neutrino fluxes from the flaring blazars in our sample is divided by  $4\pi$  and then multiplied by two factors for the completeness correction. First, the correction factor of all 4LAC blazars and the blazars of our subsample is obtained by the fraction of the total gamma-ray energy fluxes in 0.1–100 GeV (raised to the power of  $\gamma$ ) of 4LAC blazars to the sample blazars:

$$\frac{\sum_{i=1}^{N_c} (\text{Energy Flux}_i)^\gamma}{\sum_{j=1}^{N_s} (\text{Energy Flux}_j)^\gamma} \quad (8)$$

where  $N_c$  is the number of blazars in the 4LAC catalog,  $N_s$  is the number of blazars in our sample, and  $\text{Energy Flux}_{i,j}$  are time-average gamma-ray energy fluxes in 0.1–100 GeV. The second correction factor for the blazar population, which includes too distant or too low in gamma-ray luminosity sources, and the 4LAC blazars, is obtained by completeness correction factors with  $\gamma$ , which are taken from Figure 1 of Yuan et al. (2020). Since the analysis of Yuan et al. (2020) originates from the 3LAC catalog, our results are slightly conservative when applying it to the 4LAC catalog. The correction factors are presented in Table 2.

Figure 12 shows the total fluxes of muon neutrinos estimated from our bright gamma-ray FSRQs and BL Lac objects, multiplied by correction factors of the contribution of the 4LAC blazars and still unresolved blazars that are too gamma-ray faint to be included in the 4LAC catalog. The total muon neutrino fluxes of FSRQs and BL Lac objects of scenarios (1) and (2) are plotted as a function of  $\gamma$ , compared to a reference flux of the isotropic diffuse muon neutrino flux (Aartsen et al. 2016) and the three upper limits derived by Hooper et al. (2019), which are reduced to 1/3 for muon neutrinos. As the

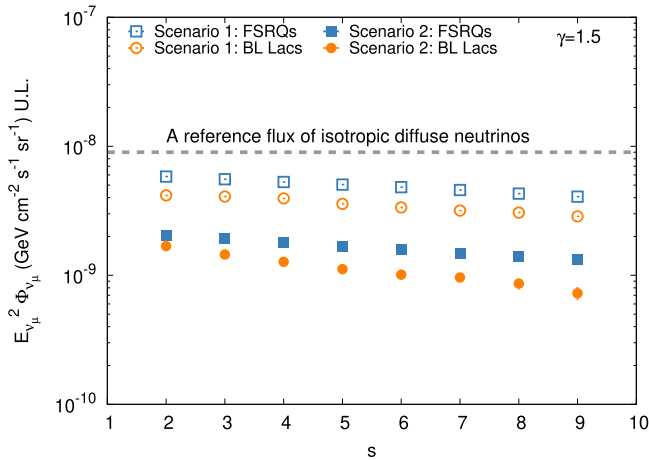


**Figure 13.** The upper limits of  $E_{\nu_\mu}^2 \Phi_{\nu_\mu}$  of a 10 yr binning as a function of the flare significance  $s$  above the quiescent level for FSRQs (open blue squares) and BL Lac objects (open orange circles) of scenario (1) and FSRQs (solid blue squares) and BL Lac objects (solid orange circles) of scenario (2) with  $\gamma = 1.5$ . The dashed horizontal line shows a reference flux of the isotropic diffuse muon neutrinos (Aartsen et al. 2016).

neutrino energy fluxes are enhanced by the weighting factor  $\gamma$ , the sum of the neutrino energy fluxes of the sample blazars gradually increases with  $\gamma$ . On the other hand, the correction factors sharply decrease with  $\gamma$  up to  $\gamma \simeq 1.5$  and stay nearly constant for  $\gamma \gtrsim 1.5$  as shown in Table 2. Therefore, the total neutrino energy fluxes, namely the product of the sum of the neutrino energy fluxes of the sample blazars and the correction factors, decrease with  $\gamma$  up to  $\gamma \simeq 1.5$  and turn to increase gradually with  $\gamma$  for  $\gamma \gtrsim 1.5$  as shown in scenario (1) of Figure 12. On the other hand, the total neutrino energy fluxes are maintained nearly constant for  $\gamma \gtrsim 1.5$  as shown in scenario (2) of Figure 12, since the gamma-ray normalization factors  $A_\gamma$  are strongly suppressed in tens of blazars shown in Figure 9 (right). The upper limits of scenario (1) are in agreement with those of Hooper et al. (2019) for  $\gamma \gtrsim 1.5$  even though the analyses and assumptions are different. We predict weaker upper limits, though, for smaller values of  $\gamma$ . This is because the second correction factor should be larger for small values of  $\gamma$  (Yuan et al. 2020). We also note that the upper limits of scenario (2) are tighter than those of scenario (1) for all values of  $\gamma$ .

So far, we have defined gamma-ray flares with the  $6\sigma$  level ( $s = 6$ ) above the quiescent gamma-ray flux. Figure 13 presents the upper-limit values of  $E_{\nu_\mu}^2 \Phi_{\nu_\mu}$  as a function of the flare significance  $s$  above the quiescent level for FSRQs and BL Lac objects in both scenarios with  $\gamma = 1.5$ . The upper limits of FSRQs and BL Lac objects are similar both for scenarios (1) and (2) with each other. The upper limits decrease with the significance levels  $s$ , becoming  $\sim 70\%$  from  $s = 2$ – $9$  for FSRQs and BL Lac objects in scenario (1).

## 5. Summary and Conclusions

We analyzed 145 bright gamma-ray blazars among the 4LAC blazars. Their flare duty cycles and energy fractions represent power-law-like distributions, correlating strongly with each other. We found a significant difference between blazar subclasses for the flare duty cycles at the 5% significant level. The flare duty cycles and energy fractions also do not correlate with the quiescent gamma-ray luminosities. Using monthly binned light curves of the 2FGL catalog,

Ackermann et al. (2011) showed that bright FSRQs and BL Lac objects have flare duty cycles of about 0.05–0.10. Our flare duty cycles of the weekly averaged time bin light curves show much broader distributions for both blazar subclasses, ranging from 0.0 to 0.6. Abdollahi et al. (2017) present the second catalog of flaring gamma-ray sources (2FAV), whose Table 2 shows the number of weekly bin flares detected for each source for the first 387 weeks of Fermi observations. According to Table 2 in Abdollahi et al. (2017), the flare duty cycles of the FAVA analysis appear to suppress less than  $\sim 0.2$ , while our flare duty cycles extend to  $\sim 0.6$ . As described in Appendix E, the photon flux distribution from the FAVA analysis is likely to systematically underestimate the flaring contribution in the total energy output of blazars. For the blazars analyzed in our sample, we find the power-law indices  $\alpha$  of the photon flux distributions are less than 2.5. This suggests that high-energy neutrinos of blazars might be produced mainly during the flare phase.

We estimated muon neutrino flare fluxes by using a scaling law of  $L_\nu^{\text{fl}} = L_\nu^q (L_\gamma^{\text{fl}}/L_\gamma^q)^\gamma$ . The quiescent neutrino flux is benchmarked with two proxies: the quiescent  $\gamma$ -ray flux and the quiescent X-ray flux with the normalization parameters of  $A_\gamma$  and  $A_X$ , whose upper limits are 1.0. By comparing the estimated muon neutrino flare fluxes to the IceCube 90% sensitivities,  $A_\gamma$  and  $A_X$  are restricted to values much lower than 1.0 for several tens of blazars. As shown in Figure 10, the predicted neutrino flaring flux for TXS 0506+056 is below the sensitivity in scenario (2), which is motivated by this source. The expected number of muon neutrinos from TXS 0506+056 is  $\sim 1$  as presented in Table 1, which is below the 90% sensitivity corresponding to  $\sim 2.4$  events.

The origin of all-sky neutrinos observed in IceCube is one of the most important puzzles in high-energy neutrino astrophysics. We found that scenarios (1) and (2) suggest that no more than  $\sim 50\%$  and  $\sim 14\%$  of the all-sky neutrino flux can originate from gamma-ray flares of FSRQs and BL Lac objects, respectively. A more realistic neutrino spectrum than the usual  $E_\nu^{-2}$  power law yields upper limits of the all-sky diffuse neutrino flux that are a factor of 2 more constraining. The upper limits are consistent with those obtained the previous literature despite different methods and assumptions.

## Acknowledgments

We thank Chengchao Yuan for providing the data of the completeness factor. K.M. is supported by the NSF grant No. AST-1908689, No. AST-2108466, and No. AST-2108467, and KAKENHI No. 20H01901 and No. 20H05852. M.P. acknowledges support from the MERAC Fondation through the project THRILL and from the Hellenic Foundation for Research and Innovation (H.F.R.I.) under the “2nd call for H.F.R.I. Research Projects to support Faculty members and Researchers” through the grant No. 3013 (UNTRAPHOB).

## Appendix A List of Our Sources

A list of the sources analyzed in this work is given in Table A1, which is available in its entirety in machine-readable form. A partial list is presented here.

**Table A1**  
List of Our Sources

4FGL Name	Object Name	RAJ2000	DEJ2000	Optical Class	SED Class	$z$
4FGL J0001.5+2113	TXS 2358+209	0.3815	21.2183	FSRQ	ISP	1.106
4FGL J0017.5-0514	PMN J0017-0512	4.3949	-5.2347	FSRQ	LSP	0.227
4FGL J0038.2-2459	PKS 0035-252	9.5652	-24.9899	FSRQ	LSP	1.196
4FGL J0102.8+5824	TXS 0059+581	15.701	58.4092	FSRQ	LSP	0.644
4FGL J0108.6+0134	4C +01.02	17.1695	1.5819	FSRQ	LSP	2.099
4FGL J0112.8+3208	4C +31.03	18.2227	32.1399	FSRQ	LSP	0.603
4FGL J0132.7-1654	PKS 0130-17	23.176	-16.9103	FSRQ	LSP	1.02
4FGL J0133.1-5201	PKS 0131-522	23.2938	-52.0202	FSRQ	LSP	0.925
4FGL J0210.7-5101	PKS 0208-512	32.6946	-51.0218	FSRQ	LSP	1.003
...	...	...	...	...	...	...

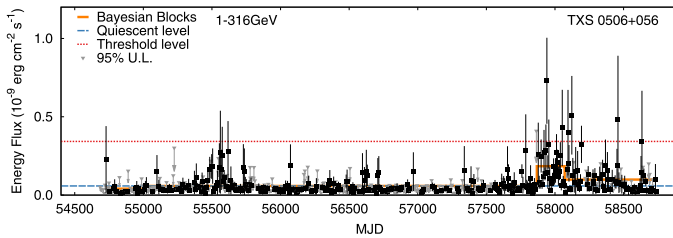
**Notes.** Optical and SED classes are from Fourth LAT AGN Catalog (4LAC) Ajello et al. (2020). Redshifts are from the 4LAC and SIMBAD Astronomical Database Oberto et al. (2019). Only a portion of this table is shown here to demonstrate its form and content. (This table is available in its entirety in machine-readable form.)

**Appendix B**

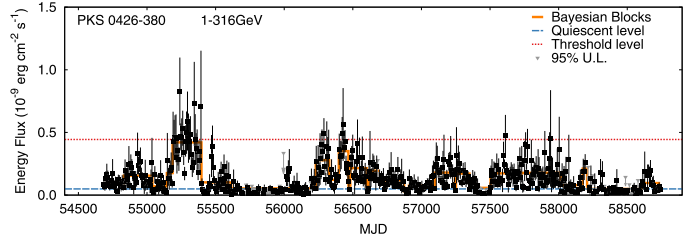
**Examples of 1–316 GeV Gamma-Ray Light Curves**

Figure B1 presents examples of weekly binned Fermi LAT light curves in the higher-energy range of 1–316 GeV (black points). The Bayesian blocks' representations and the quiescent

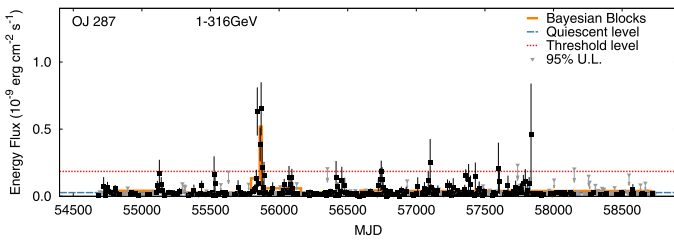
flux levels, which are derived by using the method described in Section 3.1.1, are also shown in solid orange lines and dashed cyan lines.



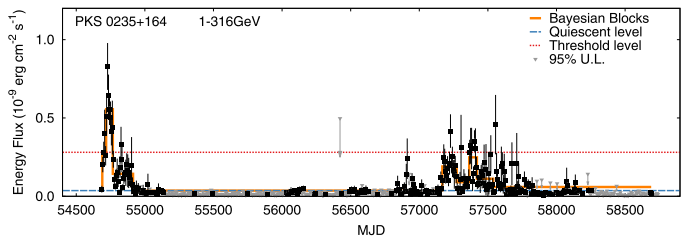
(a) TXS 0506+056



(b) PKS 0426-380



(c) OJ 287



(d) PKS 0235+164

**Figure B1.** Indicative examples of weekly binned blazar gamma-ray light curves (black points) in the 1–316 GeV energy range. Gray triangles indicate 95% upper limits. See the caption of Figure 2 in details.

### Appendix C

#### Gamma-Ray Quiescent Flux Levels with Time Binning

As mentioned in Section 3, even though there is no widely accepted agreement on how to determine the quiescent flux, it is reasonable to assume that it remains low and constant. When the gamma-ray flux is assumed to be low and constant, the quiescent gamma-ray flux does not increase with coarser time binning unless the flaring state is in effect. However, the coarser time binning should cause an increase in the quiescent gamma-ray flux, accounting for the flaring fluxes. Figure C1 presents the mean gamma-ray quiescent fluxes of 106 FSRQs, 31 BL Lac objects, and 8 BCUs with standard deviations as a function of time bins. The quiescent fluxes remain stable below  $\sim 20$  weeks and gradually increase above  $\sim 20$  weeks, indicating that they can reasonably be determined to be relatively low and constant using a 1 week time bin.

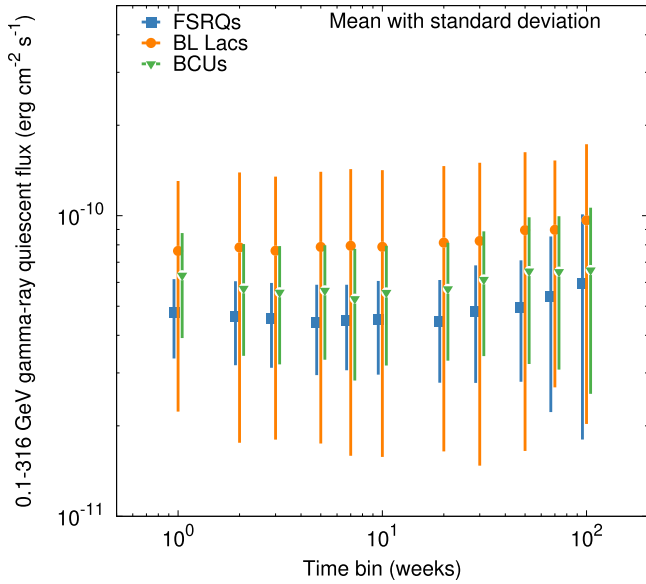
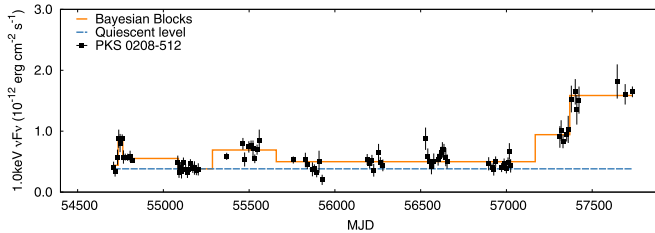


**Figure C1.** The mean gamma-ray quiescent fluxes of 106 FSRQs (blue squares), 31 BL Lac objects (orange circles), and 8 BCUs (green triangles) with the standard deviations as a function of time bins.

### Appendix D

#### X-ray Quiescent Flux Level

Examples of 1.0 keV Swift X-ray light curves are shown in Figure D1 (black points). The Bayesian blocks' representations are overplotted with solid orange lines. The quiescent flux levels are also presented with dashed cyan lines and are



(a) PKS 0208-512

estimated in the same way as for the gamma-ray quiescent flux levels —see Section 3.1.1.

### Appendix E

#### Comparison with Photon Flux Distribution Obtained by the FAVA Analysis

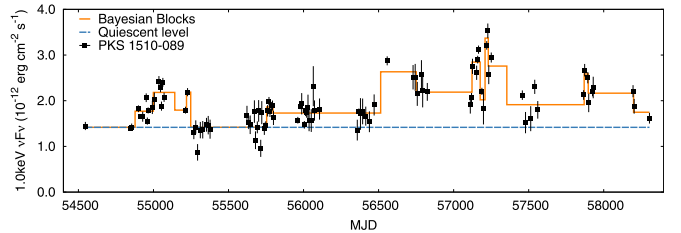
The photon flux distribution has been used to study the time variation to hold some of the important clues to the origin and nature of their variability. Murase et al. (2018) used the flux distributions with a convolution of a power law with a Poisson distribution, selecting 6 BL Lac objects at intermediate redshifts from the FAVA analysis. Their analysis indicates that the power-law index  $\alpha$  ranges from 1.7 to 3.0. However, it has been known that the FAVA analysis is not ideal for obtaining detailed information on gamma-ray light curves. Smaller values of  $\alpha$  imply the larger output of neutrinos during the flaring phase, so it is important to determine  $f_{\text{fl}}$  and  $b_{\text{fl}}^\gamma$  more precisely.

In the standard leptonic scenario for the blazar gamma-ray emission, in common, the leptonic models predict a neutrino luminosity  $L_\nu$  is in proportion to a gamma-ray luminosity  $L_\gamma$  to the power of  $\gamma \sim 1.0\text{--}2.0$  (see Murase & Waxman 2016, and references therein), giving

$$L_\nu^2 \frac{dN}{dL_\nu} \propto L_\nu^{\frac{\gamma-\alpha+1}{\gamma}}, \quad (9)$$

which implies that the flaring contribution can be dominant for the larger  $\gamma$  and smaller  $\alpha$ , e.g.,  $\gamma \geq 1.5$  and  $\alpha \leq 2.5$  (Murase et al. 2018). Thus, the index  $\alpha$  is a good indicator of the flaring contribution to the neutrino output. In this section, we compare our results of the flux distributions with those from the FAVA analysis.

Our results for several indicative sources are presented in Table E1. The source flux distribution per week is modeled as a convolution of a power law with a Poisson distribution of the source photons plus the background photons. While the number of the source photons is related to the source flux with the effective area and the exposure time, the effective area multiplied by the exposure time changes 1 week bin by 1 week bin. The number of the background photons changes as well. Hence, we include their systematic uncertainties to the fitting errors as the sum in quadrature of the errors. Figure E1 shows an example of the gamma-ray flux distributions fitted with a power-law function convolved with a Poisson distribution including the background photons, where the fitting is carried out with an unbinned maximum likelihood method. Our results on  $\alpha$ , ranging from 1.2 to 2.4, are systematically smaller than



(b) PKS 1510-089

**Figure D1.** Examples of the 1.0 keV quiescent fluxes (dashed cyan lines) of PKS 0208-512 and PKS 1510-089 X-ray light curves (black points) with the Bayesian block representations (orange solid lines).

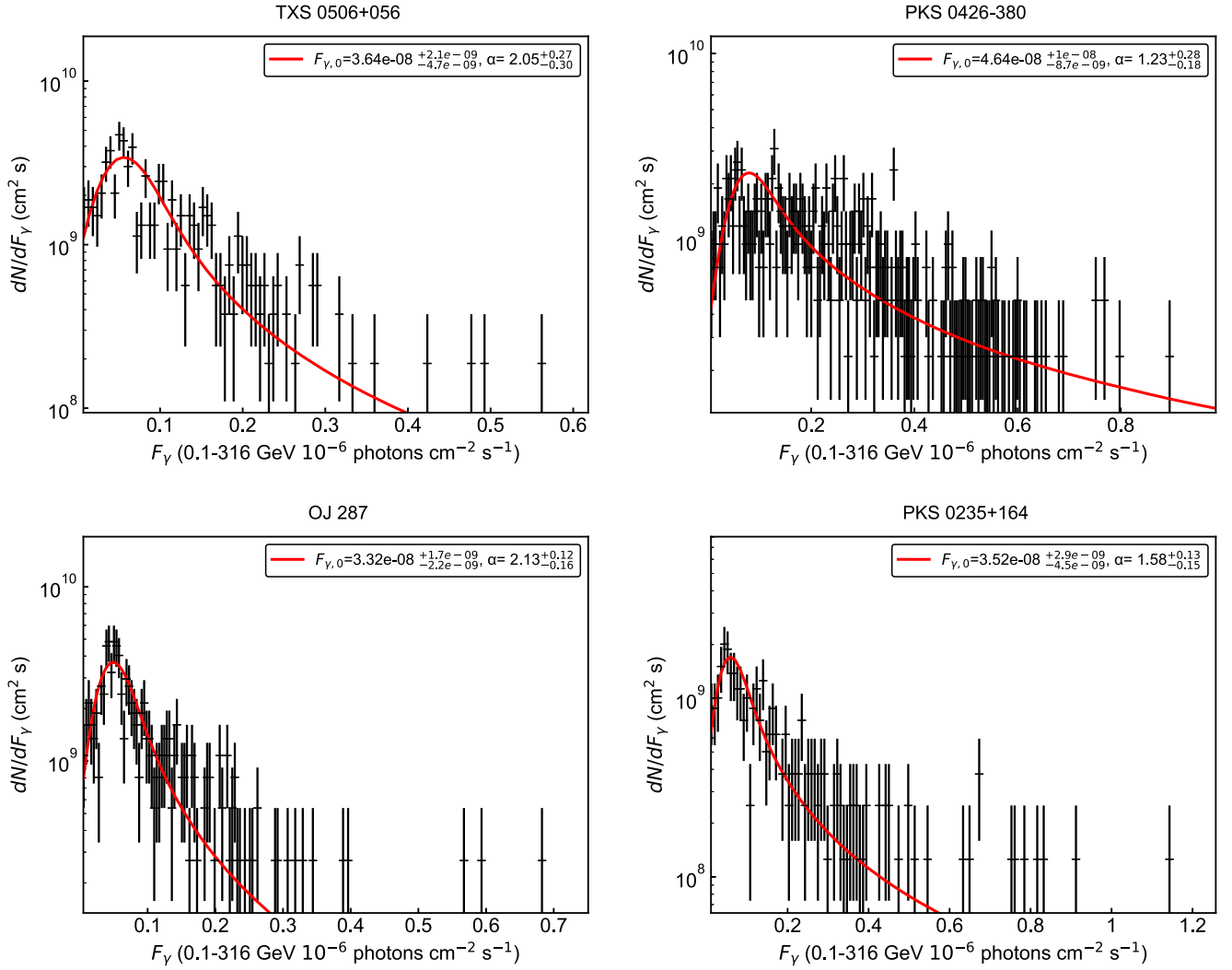


**Figure E1.** The gamma-ray flux distributions of TXS 0506+056, PKS 0426-380, OJ 287, and PKS 0235+164 in 0.1–316 GeV fitted with a power-law function convolved with a Poisson distribution including the background photons. See text for details.

**Table E1**

Gamma-ray Flare Duty Cycle ( $f_{\text{fl}}$ ), Flare Energy Fraction ( $b_{\text{fl}}^{\gamma}$ ), and Best-fit Power-law Index of the Flux Distribution ( $\alpha$ ) for a Few Indicative Sources from Our Sample

Name	$f_{\text{fl}}$	$b_{\text{fl}}^{\gamma}$	$f_{\text{fl}}^{\text{LE}}$	$b_{\text{fl}}^{\text{LE}}$	$f_{\text{fl}}^{\text{HE}}$	$b_{\text{fl}}^{\text{HE}}$	$\alpha$	$\alpha^{\text{HE}}$
TXS 0506+056	$0.014 \pm 0.002$	$0.055 \pm 0.011$	$0.009 \pm 0.002$	$0.039 \pm 0.009$	$0.038 \pm 0.004$	$0.132 \pm 0.016$	$2.05^{+0.27}_{-0.31}$	$2.82^{+0.15}_{-0.16}$
PKS 0426-380	$0.164 \pm 0.008$	$0.364 \pm 0.020$	$0.136 \pm 0.008$	$0.322 \pm 0.019$	$0.152 \pm 0.008$	$0.343 \pm 0.020$	$1.23^{+0.28}_{-0.18}$	$2.18^{+0.43}_{-0.20}$
OJ 287	$0.031 \pm 0.004$	$0.115 \pm 0.015$	$0.029 \pm 0.004$	$0.110 \pm 0.015$	$0.023 \pm 0.003$	$0.113 \pm 0.019$	$2.13^{+0.12}_{-0.16}$	$2.84^{+0.18}_{-0.19}$
PKS 0235+164	$0.059 \pm 0.005$	$0.183 \pm 0.017$	$0.051 \pm 0.005$	$0.165 \pm 0.017$	$0.070 \pm 0.006$	$0.212 \pm 0.019$	$1.58^{+0.13}_{-0.15}$	$1.87^{+0.13}_{-0.09}$
PKS 0301-243	$0.014 \pm 0.002$	$0.076 \pm 0.016$	$0.010 \pm 0.002$	$0.067 \pm 0.016$	$0.009 \pm 0.002$	$0.058 \pm 0.017$	$2.43^{+0.21}_{-0.22}$	$3.15^{+0.43}_{-0.16}$
S5 0716+71	$0.290 \pm 0.011$	$0.507 \pm 0.021$	$0.221 \pm 0.010$	$0.415 \pm 0.020$	$0.224 \pm 0.010$	$0.463 \pm 0.022$	$1.43^{+0.19}_{-0.13}$	$2.15^{+0.13}_{-0.12}$
S4 0954+65	$0.024 \pm 0.003$	$0.114 \pm 0.018$	$0.021 \pm 0.003$	$0.104 \pm 0.018$	$0.021 \pm 0.003$	$0.138 \pm 0.024$	$2.37^{+0.13}_{-0.17}$	$2.51^{+0.22}_{-0.17}$

**Note.** Values are reported for a low-energy range (LE: 0.1–1 GeV), a high-energy range (HE: 1–316 GeV), and the full LAT energy range (0.1–316 GeV). The flaring threshold level is defined in Equation (1) with  $s = 6$ .

those of FAVA analysis, which range from 1.7 to 3.0 (Murase et al. 2018). Hence, the photon flux distribution from the FAVA analysis tends to underestimate the flaring contribution to the neutrino output of a blazar, and our results would better justify the “flare dominance” in neutrino emission, considered by Murase et al. (2018).

## Appendix F Estimated Muon Neutrino Flare Fluxes by Using the Gamma-Ray Photon Fluxes

Figure F1 shows the estimated muon neutrino flare fluxes from the gamma-ray photon fluxes for a 1 week bin (a) and a 10 yr bin (b) of scenario (1) with  $A_{\gamma} = 1.0$ , and  $\gamma = 1.5$  as a

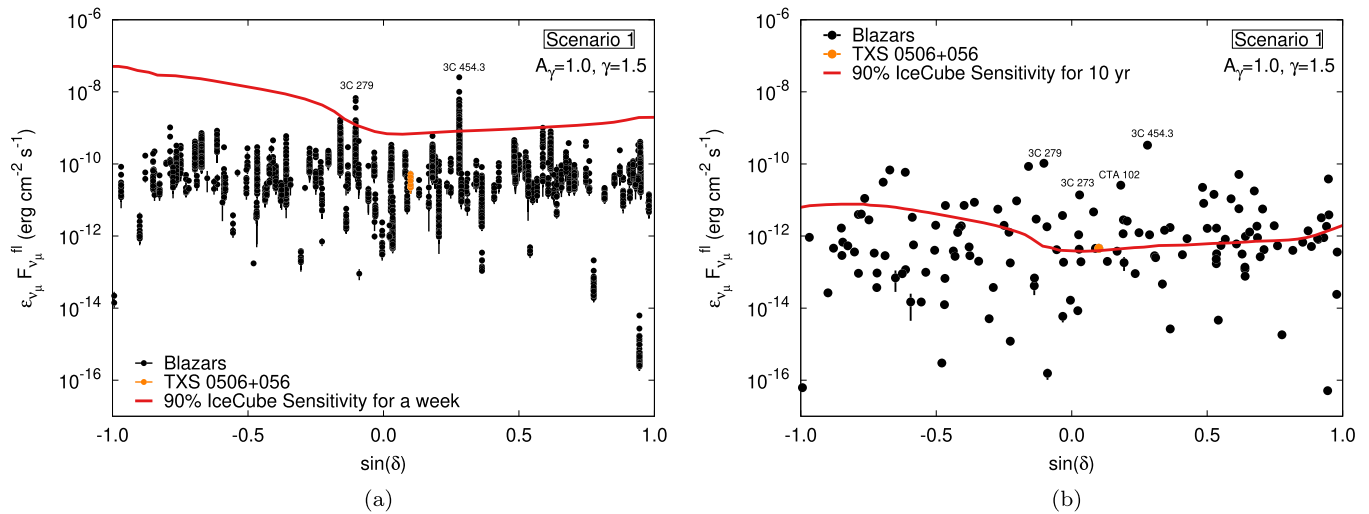


**Figure F1.** Estimated muon neutrino flare fluxes of 136 blazars (101 FSRQs, 28 BL Lac objects, and 7 BCUs) from the gamma-ray photon fluxes for a 1 week bin (a) and a 10 yr bin (b) of scenario (1) with  $A_\gamma = 1.0$ , and  $\gamma = 1.5$  as a function of  $\sin(\delta)$ . The 90% IceCube sensitivities are the same as in Figure 8.

function of  $\sin(\delta)$ . As seen by comparing Figure F1 with Figure 8, the estimated muon neutrino fluxes of the gamma-ray photon fluxes are almost similar to those of the gamma-ray energy fluxes.

### ORCID iDs

Kenji Yoshida <https://orcid.org/0000-0001-6813-2665>  
 Maria Petropoulou <https://orcid.org/0000-0001-6640-0179>  
 Kohta Murase <https://orcid.org/0000-0002-5358-5642>  
 Foteini Oikonomou <https://orcid.org/0000-0002-0525-3758>

### References

- Aartsen, M. G., Abbasi, R., Abdou, Y., et al. 2013a, *PhRvL*, **111**, 021103  
 Aartsen, M. G., Abbasi, R., Abdou, Y., (IceCube Collaboration), et al. 2013b, *Sci*, **342**, 1242856  
 Aartsen, M. G., Abraham, K., Ackermann, M., et al. 2015a, *PhRvL*, **115**, 081102  
 Aartsen, M. G., Abraham, K., Ackermann, M., et al. 2016, *ApJ*, **833**, 3  
 Aartsen, M. G., Abraham, K., Ackermann, M., et al. 2017a, *ApJ*, **835**, 45  
 Aartsen, M. G., Abraham, K., Ackermann, M., et al. 2017b, *ApJ*, **835**, 151  
 Aartsen, M. G., Ackermann, M., Adams, J., et al. 2014, *ApJ*, **796**, 109  
 Aartsen, M. G., Ackermann, M., Adams, J., et al. 2015b, *ApJ*, **807**, 46  
 Aartsen, M. G., Ackermann, M., Adams, J., et al. 2020a, *PhRvL*, **125**, 121104  
 Aartsen, M. G., Ackermann, M., Adams, J., et al. 2020b, *PhRvL*, **124**, 051103  
 Abbasi, R., Ackermann, M., Adams, J., et al. 2022, *ApJ*, **938**, 38  
 Abdullahi, S., Acero, F., Ackermann, M., et al. 2020, *ApJS*, **247**, 33  
 Abdullahi, S., Ackermann, M., Ajello, M., et al. 2017, *ApJ*, **846**, 34  
 Ackermann, M., Ajello, M., Allafort, A., et al. 2011, *ApJ*, **743**, 171  
 Ahlers, M., & Halzen, F. 2017, *PTEP*, **2017**, 12A105  
 Ajello, M., Angioni, R., Axelsson, M., et al. 2020, *ApJ*, **892**, 105  
 Albert, A., André, M., Anghinolfi, M., et al. 2018, *ApJL*, **868**, L20  
 Astropy Collaboration, Price-Whelan, A. M., & Sipőcz, B. M. 2018, *AJ*, **156**, 123  
 Astropy Collaboration, Robitaille, T. P., Tollerud, E. J., et al. 2013, *A&A*, **558**, A33  
 Atwood, W. B., Abdo, A. A., Ackermann, M., et al. 2009, *ApJ*, **697**, 1071  
 Buson, S., Tramacere, A., Pfeiffer, L., et al. 2022, *ApJL*, **933**, L43  
 Capel, F., Mortlock, D. J., & Finley, C. 2020, *PhRvD*, **101**, 123017  
 Costamante, L. 2020, *MNRAS*, **491**, 2771  
 Dermer, C. D., Murase, K., & Inoue, Y. 2014, *JHEAp*, **3**, 29  
 Gao, S., Pohl, M., & Winter, W. 2017, *ApJ*, **843**, 109  
 Giommi, P., Brandt, C. H., Barres de Almeida, U., et al. 2019, *A&A*, **631**, A116  
 Hooper, D., Linden, T., & Vieregge, A. 2019, *JCAP*, **2019**, 012  
 Hovatta, T., Lindfors, E., Kiehlmann, S., et al. 2021, *A&A*, **650**, A83  
 IceCube Collaboration, Aartsen, M. G., Ackermann, M., et al. 2018a, *Sci*, **361**, eaat1378  
 IceCube Collaboration, Aartsen, M. G., Ackermann, M., et al. 2018b, *Sci*, **361**, 147  
 Kadler, M., Krauß, F., Mannheim, K., et al. 2016, *NatPh*, **12**, 807  
 Keivani, A., Murase, K., Petropoulou, M., et al. 2018, *ApJ*, **864**, 84  
 Mészáros, P. 2017, *ARNPS*, **67**, 45  
 Meyer, M., Scargle, J. D., & Blandford, R. D. 2019, *ApJ*, **877**, 39  
 Murase, K. 2017, in *Neutrino Astronomy: Current Status, Future Prospects.*, ed. T. Gaisser & A. Karle (Singapore: World Scientific), 15  
 Murase, K., Ahlers, M., & Lacki, B. C. 2013, *PhRvD*, **88**, 121301  
 Murase, K., Guetta, D., & Ahlers, M. 2016, *PhRvL*, **116**, 071101  
 Murase, K., Inoue, Y., & Dermer, C. D. 2014, *PhRvD*, **90**, 023007  
 Murase, K., Oikonomou, F., & Petropoulou, M. 2018, *ApJ*, **865**, 124  
 Murase, K., & Stecker, F. W. 2022, arXiv:2202.03381  
 Murase, K., & Waxman, E. 2016, *PhRvD*, **94**, 103006  
 Nalewajko, K. 2013, *MNRAS*, **430**, 1324  
 Neronov, A., Semikoz, D. V., & Ptitsyna, K. 2017, *A&A*, **603**, A135  
 Oberto, A., Allen, M., Loup, C., & Lesteven, S. 2019, in *ASP Conf. Ser. 521*, *Astronomical Data Analysis Software and Systems XXVI*, ed. M. Molinaro, K. Shorridge, & F. Pasian (San Francisco, CA: ASP), 96  
 Oikonomou, F., Murase, K., Padovani, P., Resconi, E., & Mészáros, P. 2019, *MNRAS*, **489**, 4347  
 Oikonomou, F., Petropoulou, M., Murase, K., et al. 2021, *JCAP*, **10**, 082  
 Padovani, P., Petropoulou, M., Giommi, P., & Resconi, E. 2015, *MNRAS*, **452**, 1877  
 Paliya, V. S., Böttcher, M., Olmo-García, A., et al. 2020, *ApJ*, **902**, 29  
 Palladino, A., Rodrigues, X., Gao, S., & Winter, W. 2019, *ApJ*, **871**, 41  
 Petropoulou, M., Coenders, S., & Dimitrakoudis, S. 2016, *Aph*, **80**, 115  
 Petropoulou, M., Dimitrakoudis, S., Padovani, P., Mastichiadis, A., & Resconi, E. 2015, *MNRAS*, **448**, 2412  
 Petropoulou, M., Murase, K., Santander, M., et al. 2020, *ApJ*, **891**, 115  
 Petropoulou, M., Oikonomou, F., Mastichiadis, A., et al. 2020, *ApJ*, **899**, 113  
 Plavin, A. V., Kovalev, Y. Y., Kovalev, Y. A., & Troitsky, S. V. 2021, *ApJ*, **908**, 157  
 Resconi, E., Franco, D., Gross, A., Costamante, L., & Flaccomio, E. 2009, *A&A*, **502**, 499  
 Rodrigues, X., Garrappa, S., Gao, S., et al. 2021, *ApJ*, **912**, 54  
 Sahakyan, N., Giommi, P., Padovani, P., et al. 2022, *MNRAS*, **519**, 1396  
 Scargle, J. D., Norris, J. P., Jackson, B., & Chiang, J. 2013, *ApJ*, **764**, 167  
 Smith, D., Hooper, D., & Vieregge, A. 2021, *JCAP*, **2021**, 031  
 Stathopoulos, S. I., Petropoulou, M., Giommi, P., et al. 2022, *MNRAS*, **510**, 4063  
 Urry, C. M., & Padovani, P. 1995, *PASP*, **107**, 803  
 Vandenbroucke, J., Pizzuto, A., & Meagher, K. 2019, in *36th Int. Cosmic Ray Conf. (ICRC2019)*, ed. P. Desiati et al. (Trieste: SISSA), 1026  
 Wood, M., Caputo, R., Charles, E., et al. 2017, in *35th Int. Cosmic Ray Conf.*, ed. P. II Heung (Trieste: SISSA), 824  
 Yuan, C., Murase, K., & Mészáros, P. 2020, *ApJ*, **890**, 25  
 Zhou, B., Kamionkowski, M., & Liang, Y.-F. 2021, *PhRvD*, **103**, 123018